iScience

CellPress
OPEN ACCESS

Article

Complex sphingolipid profiling and identification of an inositol-phosphorylceramide synthase in *Dictyostelium discoideum*

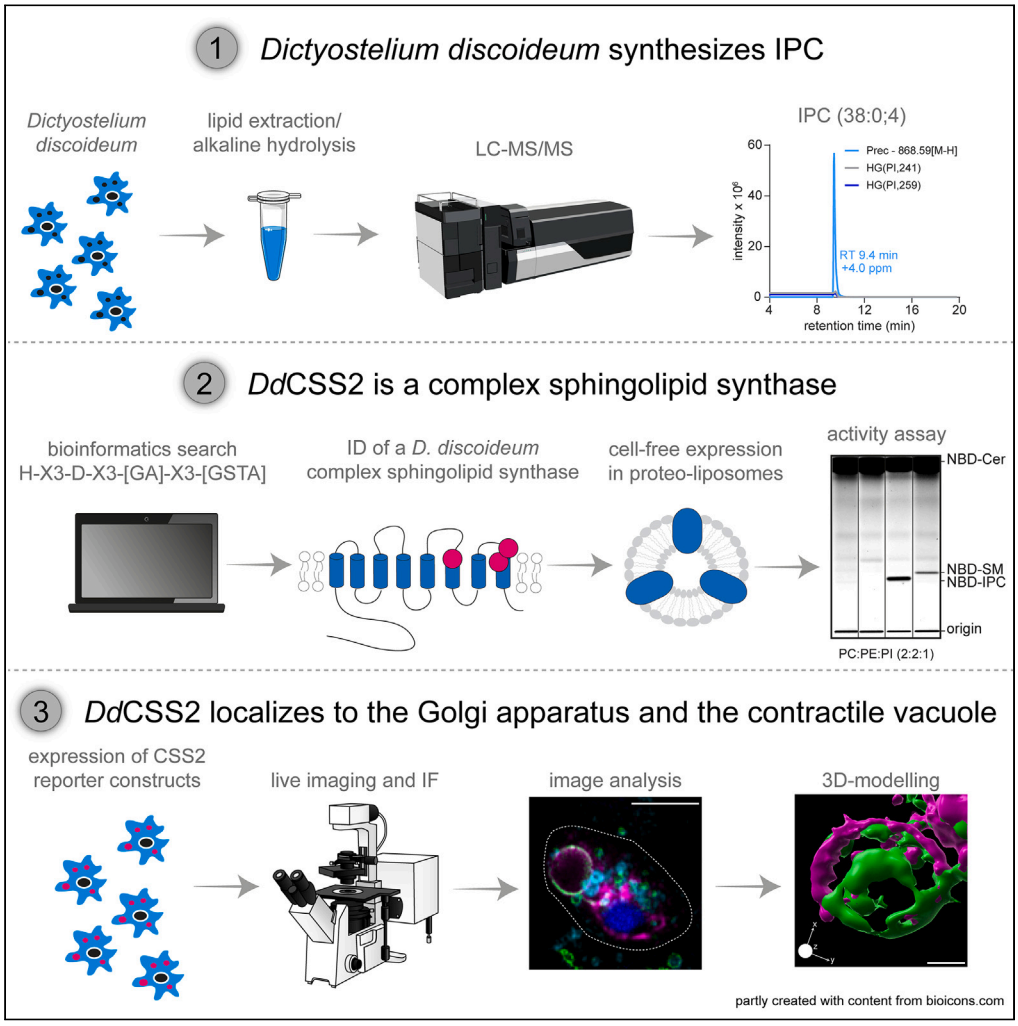

Stevanus A. Listian, Anna-Carina Mazur, Matthijs Kol, ..., Stefan Walter, Joost C.M. Holthuis, Caroline Barisch

caroline.barisch@cssb-hamburg.de

Highlights

Dictyostelium discoideum produces phosphoinositol-containing sphingolipids

*Dd*CSS2 shares structural features with inositol-phosphorylceramide (IPC) synthases

*Dd*CSS2 shows IPC synthase activity

*Dd*CSS2 is found in both, the Golgi apparatus and the contractile vacuole

Listian et al., iScience *27*, 110609
September 20, 2024
https://doi.org/10.1016/j.isci.2024.110609

iScience

CellPress
OPEN ACCESS

Article

Complex sphingolipid profiling and identification of an inositol-phosphorylceramide synthase in *Dictyostelium discoideum*

Stevanus A. Listian,[1] Anna-Carina Mazur,[1,5,6,7] Matthijs Kol,[2,4] Edwin Ufelmann,[1] Sebastian Eising,[3] Florian Fröhlich,[3,4] Stefan Walter,[4] Joost C.M. Holthuis,[2,4] and Caroline Barisch[1,4,5,6,7,8,*]

SUMMARY

***Dictyostelium discoideum* is a professional phagocyte frequently used to study cellular processes underlying the recognition, engulfment, and infection course of microbial pathogens. Sphingolipids are abundant components of the plasma membrane that bind cholesterol, control membrane properties, participate in signal transmission, and serve as adhesion molecules in recognition processes relevant to immunity and infection. By combining lipidomics with a bioinformatics-based cloning strategy, we show here that *D. discoideum* produces phosphoinositol-containing sphingolipids with predominantly phytoceramide backbones. Cell-free expression of candidate inositol-phosphorylceramide (IPC) synthases from *D. discoideum* enabled identification of an enzyme that selectively catalyzes the transfer of phosphoinositol from phosphatidylinositol onto ceramide. The IPC synthase, *Dd*IPCS1, shares multiple sequence motifs with yeast IPC and human sphingomyelin synthases and localizes to the Golgi apparatus as well as the contractile vacuole of *D. discoideum*. These findings open up important opportunities for exploring a role of sphingolipids in phagocytosis and infection across major evolutionary boundaries.**

INTRODUCTION

Sphingolipids are a structurally diverse class of lipids with properties essential for the evolution of eukaryotic cells. They typically represent ~ 15% of cellular lipids and are highly enriched in the plasma membrane (PM) where they modulate key physical membrane properties, including fluidity, thickness, and curvature.[1,2] Their affinity for cholesterol and ability to self-associate into laterally segregated membrane microdomains control a variety of membrane proteins including signaling receptors.[3,4] Besides their vital roles as structural components of cellular membranes, sphingolipids, and in particular intermediates of sphingolipid metabolism, function as signaling molecules that regulate a variety of biological processes, ranging from cell proliferation, cell death, and cell migration to neurotransmission, angiogenesis, and inflammation.[5,6]

The common feature of sphingolipids is a long-chain base (LCB), predominantly sphingosine in animals and phytosphingosine in plants and fungi.[7,8] N-acylation of the LCB with a long-chain fatty acid generates ceramide (Cer), a central intermediate of sphingolipid metabolism.[9] Addition of a polar head group to the primary hydroxyl group of Cer gives rise to complex sphingolipids. Based on their head group composition, complex sphingolipids can be grouped into phosphosphingolipids and glycosphingolipids. However, these categories are not mutually exclusive. Plants and fungi, for example, add phosphoinositol to phytoceramide to generate IPC, after which the inositol-containing head can be further decorated with one or more monosaccharides.[10] While core features of the sphingolipid biosynthetic pathway and the subcellular organization of the underlying enzymatic machinery are conserved among eukaryotes,[11,12] organisms across different evolutionary branches generate complex sphingolipids with distinct polar head groups. For instance, plants and fungi generate IPC[8,10] whereas mammals and nematodes produce phosphocholine-containing sphingomyelin (SM).[13–15] In contrast, insects like *Drosophila melanogaster* and some protozoa predominantly synthesize ethanolamine-phosphorylceramide (EPC).[16–21]

Analogous to members of the lipid phosphate phosphatase (LPP) superfamily, known SM and IPC synthases are polytopic membrane proteins with an active site comprising a conserved catalytic triad of two histidine residues and one aspartate.[22,23] These residues participate in cleavage of the bond between the lipid hydroxyl and phosphate groups of the head group donor, phosphatidylinositol (PI) in the case of yeast IPC synthase, thus enabling the transfer of inositolphosphate from PI onto phytoceramide to produce IPC, releasing diacylglycerol as a side

[1]Division of Molecular Infection Biology, Department of Biology/Chemistry, University of Osnabrück, Osnabrück, Germany
[2]Division of Molecular Cell Biology, Department of Biology/Chemistry, University of Osnabrück, Osnabrück, Germany
[3]Division of Molecular Membrane Biology, Department of Biology/Chemistry, University of Osnabrück, Osnabrück, Germany
[4]Center of Cellular Nanoanalytics (CellNanOs), University of Osnabrück, Osnabrück, Germany
[5]Centre for Structural Systems Biology, Hamburg, Germany
[6]Division of Host-Microbe Interactome, Research Center Borstel (FZB) - Leibniz Lung Center, Borstel, Germany
[7]Department of Biology, University of Hamburg, Hamburg, Germany
[8]Lead contact
*Correspondence: caroline.barisch@cssb-hamburg.de
https://doi.org/10.1016/j.isci.2024.110609

product. Animal SM synthases follow a similar LPP-type reaction cycle to produce SM, using phosphatidylcholine (PC) as head group donor. Besides sharing LPP-like sequence motifs, yeast IPC and animal SM synthases lack any obvious sequence homology.[23]

The ameba *D. discoideum* is an attractive model organism for cell biological research. Due to its relative simplicity and genetic tractability, it is particularly attractive for investigating fundamental processes including chemotaxis, phagocytosis, and autophagy. In infection biology, *D. discoideum* is frequently used as a surrogate host macrophage to investigate the pathogenesis of various microorganisms, including mycobacteria, *Legionella pneumophila*, *Pseudomonas aeruginosa*, and *Cryptococcus neoformans*. Apart from its importance for infection research, *D. discoideum* is also a versatile tool to study the cell biology of lipids. For example, recent work revealed that *D. discoideum* primarily utilizes ether-linked inositol phospholipids for signaling[24] and that ether lipids play an important role during phagocytosis.[25] We previously demonstrated that intracellular mycobacteria use *D. discoideum* triacylglycerols and phospholipids as major carbon and energy sources.[26,27] Despite its wide acceptance as a model organism, the sphingolipidome of *D. discoideum* remains poorly characterized and many of the sphingolipid biosynthetic enzymes are yet to be identified. *D. discoideum* emerged after the plant-animal split and is evolutionary close to both *S. cerevisiae* and humans.[28] Despite *D. discoideum*'s earlier divergence, several of its proteins are more comparable to human orthologs than those of *S. cerevisiae*, most likely due to faster rates of evolutionary change along the fungal lineage.[28] As consequence, it is also difficult to pin down the specific lipid species produced by this organism. Elucidating the sphingolipid profile of this organism would offer valuable insights into the evolution of both sphingolipid biosynthesis and function.

Here, we conducted BLAST searches with sequences of previously identified sphingolipid biosynthetic enzymes to reconstruct the sphingolipid biosynthetic pathway in *D. discoideum*. As this approach did not yield any clue on the nature of complex sphingolipids in *D. discoideum*, we carried out mass spectrometry (MS)-based profiling of its sphingolipidome. This revealed that, analogous to plants and fungi, *D. discoideum* produces IPC. A bioinformatics-based search for candidate IPC synthases in *D. discoideum* coupled to their functional analysis in a cell-free expression system yielded a polytopic membrane protein, which catalyzes the transfer of phosphoinositol from PI onto ceramide to generate IPC. Localization studies showed that this protein resides in the Golgi apparatus and contractile vacuole (CV) of *D. discoideum*.

RESULTS

Reconstruction of the sphingolipid biosynthetic pathway in *D. discoideum*

While sphingolipids are ubiquitous among eukaryotes, the pathway of *de novo* sphingolipid biosynthesis in *D. discoideum* has remained largely unexplored. This led us to search the *D. discoideum* database for homologs of key sphingolipid biosynthetic enzymes previously identified in *A. thaliana*,[29] *S. cerevisiae*,[30] and *H. sapiens*[31](Figure 1, Table S1). The first committed and rate-limiting step of sphingolipid synthesis is the condensation of serine and palmitoyl-CoA, a reaction catalyzed by serine-palmitoyltransferase (SPT) yielding ketodihydrosphingosine or 3-ketosphinganine (3-KDS) (Figure 1). In eukaryotes, SPT comprises a core heterodimer of two large catalytic subunits and two accessory small subunits (ssSPT). While the genome of *D. discoideum* encodes homologs of the two large catalytic subunits (SptA and SptB; Table 1), we were unable to identify any ssSPT homolog. SPT forms a so-called SPOTS complex with the regulatory orosomucoid (Orm) proteins and the phosphatidylinositol-4-phosphate phosphatase Sac1. *D. discoideum* appears to have only one Orm-like protein (dictybase: DDB_G0288847), and we found two structural homologs of Sac1 (Sac1 and Sac1-like). A recent study revealed the cryo-EM structure of the Cer-bound SPOTS complex in yeast and provided evidence for the presence of a Sac1-containing SPOTS complex in *D. discoideum*.[30] SPT gives rise to 3-KDS, which is then further reduced to sphinganine (dihydrosphingosine) by 3-ketosphinganine reductase (Ksr). In *D. discoideum*, there are two identical copies of this enzyme in AX3 and AX4 (but not AX2), known as KsrA-1 and KsrA-2. Sphinganines are then converted into dihydroceramides by Cer synthases (CerS) through the addition of fatty acid moieties. Mammals, plants and yeast each contain three to six CerS isoforms that produce dihydroceramides with distinct acyl chain lengths.[32–34] This is in sharp contrast to *D. discoideum*, which contains only one CerS homolog (CrsA).[35] Dihydrosphingosines and dihydroceramides are generally further modified by desaturases and hydroxylases. BLAST (https://blast.ncbi.nlm.nih.gov) searches for *D. discoideum* homologs of the yeast sphinganine C4-hydroxylase Sur2 produced three hits, here referred to as lipid hydroxylase LhsA, LhsB, and LhsC. Sphingolipid desaturases are present in human[36] and *A. thaliana*[37,38] but absent in *S. cerevisiae*.[39] In *D. discoideum* we found one dihydroceramide desaturase homolog (DesA). The amide-linked acyl chain in sphingolipids usually undergoes further hydroxylations. A search for *D. discoideum* homologs of the yeast Cer fatty acid hydroxylase Scs7 and the *A. thaliana* Cer fatty acid hydroxylases FAH1 and FAH2 in each case yielded one hit, namely LhsD.

Collectively, these results indicate that *D. discoideum* has the capacity to produce Cers with a desaturated LCB and carrying hydroxyl groups in both the LCB and amide-linked acyl chain. Cers can be further derivatized by addition of a head group at C1 to generate complex sphingolipids like glucosylceramide (GlcCer), the precursor of complex glycosphingolipids that contain a few to dozens of sugar residues. Alternatively, the C1 of Cer can be modified with a phospho-alcohol to generate SM, EPC, or IPC. A search for *D. discoideum* homologs of GlcCer synthases in *Homo sapiens* (*Hs*CEGT), *Candida albicans* (*Ca*CEGT), or *A. thaliana* (*At*CEGT) did not produce any hits. BLAST searches using sequences of the enzymes responsible for the production of SM (*Hs*SMS1), EPC (*Hs*SMSr), or IPC (*Sc*Aur1, *At*IPCS1) produced several hits in each case but failed to identify clear homologs in *D. discoideum*. Consequently, our homology searches did not yield further insights into the nature of the complex sphingolipids produced by *D. discoideum*.

Phosphatidylethanolamine is the most abundant phospholipid in *D. discoideum*

The synthesis of complex phosphosphingolipids involves the transfer of the polar head group from a phospholipid donor such as PC, phosphatidylethanolamine (PE) or PI onto C1 of Cer. Interestingly, eukaryotic organisms evolved different head group dominances regarding their phospholipid and sphingolipid production. To determine the head group dominance in *D. discoideum*, we performed an untargeted

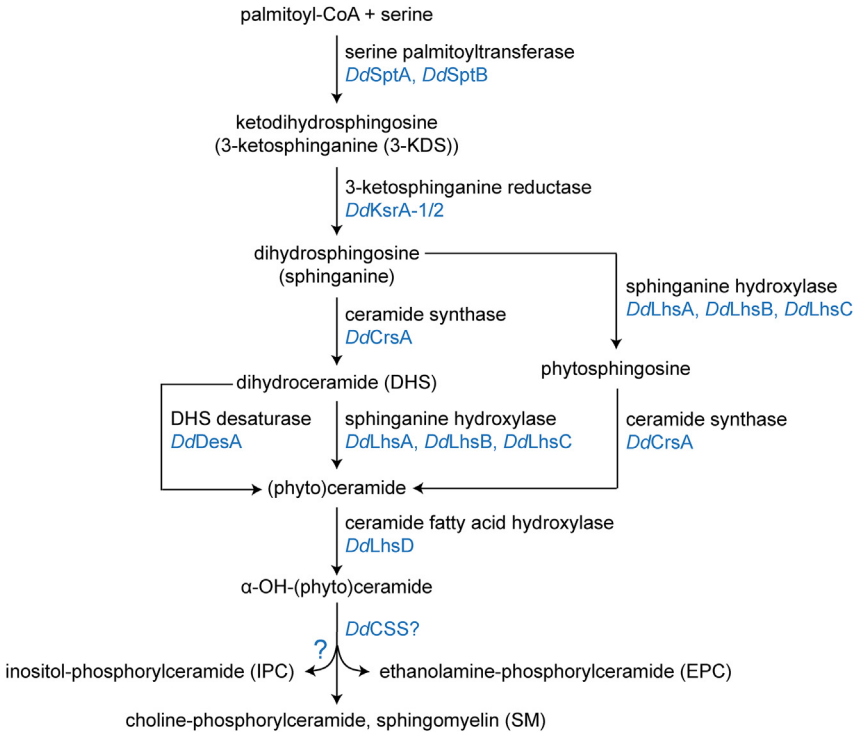

Figure 1. The sphingolipid biosynthetic pathway in *D. discoideum*

The pathway was reconstructed based on BLAST searches for *D. discoideum* homologs (marked in blue) of key sphingolipid biosynthetic enzymes identified in *S. cerevisiae*, *A. thaliana*, and *H. sapiens* (Table S1). Note that this approach did not yield clear *D. discoideum* homologs of complex sphingolipid synthases (CSS) responsible for the production of inositol-phosphorylceramide (IPC), ethanolamine-phosphorylceramide (EPC), or sphingomyelin (SM) in fungi, plants, or animals.

LC-MS/MS analysis of total lipid extracts from *D. discoideum* cultured in defined medium (SIH, Formedium). We found that PE is by far the most prevalent lipid class in *D. discoideum*, representing ~70 mol % of all lipids analyzed, with PC and PI representing ~10 mol % and ~7 mol %, respectively (Figure 2A, Table S2). Besides, diacylphospholipids (~88.7 mol %), *D. discoideum* contains substantial amounts of lysophospholipids (~6.8 mol %), notably lysophosphatidyl-ethanolamine (LPE), as well as Cers (~0.6 mol %), diacylglycerol (DAG, ~2.3 mol %), and triacylglycerols (TAG; ~1.6 mol %) (Figure 2A).

Phospholipids have either an ester or an ether bond at the *sn*-1 position. Figure 2B provides molecular structures of an ester lipid (diacyl PI) and an ether lipid (alkyl-acyl PI). In *D. discoideum*, the majority of inositol phospholipids are ether lipids with a novel plasmanyl-*O*-34:1

Table 1. Sphingolipid biosynthetic enzymes in *D. discoideum*, *A. thaliana*, *S. cerevisiae* and *H. sapiens*

Enzyme	*D. discoideum*	*A. thaliana*	*S. cerevisiae*	*H. sapiens*
serine palmitoyltransferase (large subunits)	SptA (DDB_G0268056), SptB (DDB_G0291283)	LCB1, LCB2a, LCB2b	Lcb1, Lcb2	SPTLC1, SPTLC2, SPTLC3
3-ketodihydrosphingosine reductase	KsrA-1 (DDB_G0274015), KsrA-2 (DDB_G0272883)	KSR1, KSR2	Tsc10	KDSR
sphingolipid desaturase	DesA (DDB_G0269738)	SLD1, SLD2, DES1	non-existent	DEGS1
ceramide synthase	CrsA (DDB_G0282607)	LOH1, LOH2, LOH3	Lac1, Lag1, Lip1	CERS1, CERS2, CERS3, CERS4, CERS5, CERS6
sphingolipid hydroxylase	LhsA (DDB_G0269788), LhsB (DDB_G0270946), LhsC (DDB_G0279611)	SBH1, SBH2	Sur2	DES2
ceramide acyl hydroxylase	LhsD (DDB_G0269908)	FAH1, FAH2	Scs7	non-existent

Putative sphingolipid biosynthetic enzymes from *D. discoideum* (www.dictybase.org) were confirmed by BLAST search analysis using sequences of *A. thaliana*, *S. cerevisiae*, and *H. sapiens* as bait. The putative lipid hydroxylases are not yet annotated at dictybase and were named here LhsA (dictybase: DDB_G0269788), LhsB (dictybase: DDB_G0270946), LhsC (dictybase: DDB_G0279611), and LhsD (dictybase: DDB_G0269908). For more information, please see Table S1.

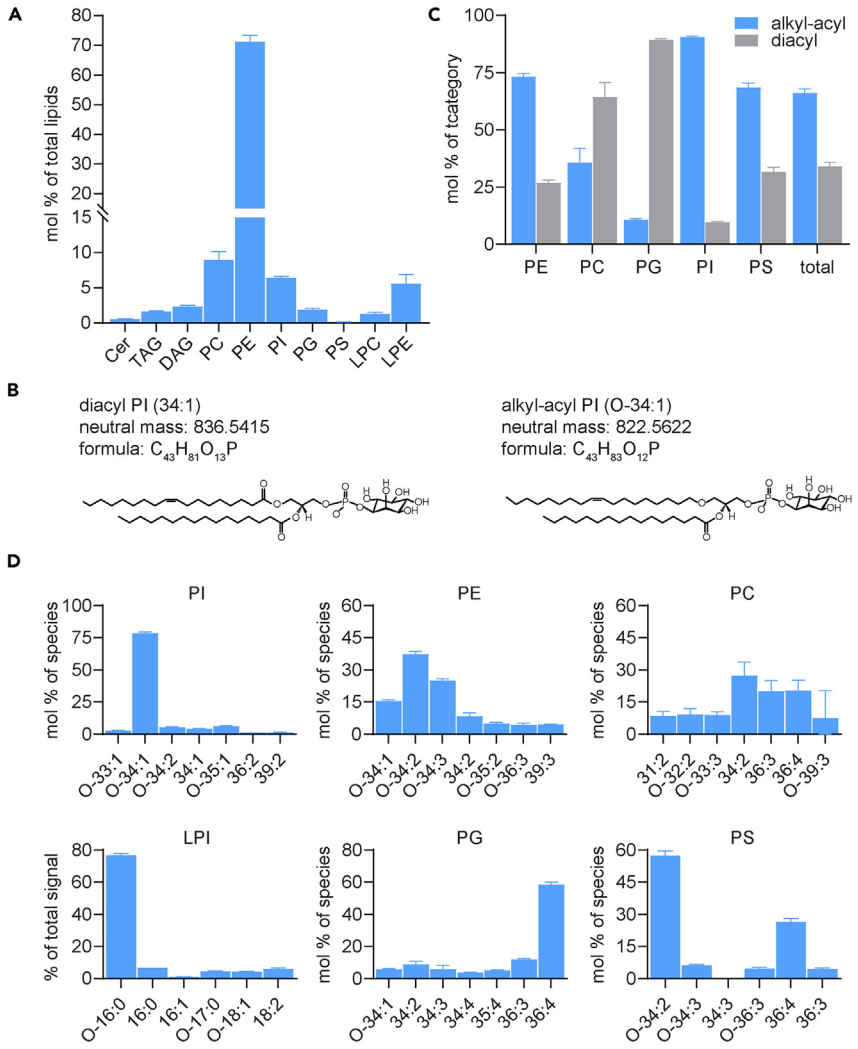

Figure 2. Quantitative analysis of the main lipid classes in *D. discoideum*

(A) Levels of indicated lipid classes in total lipid extracts from *D. discoideum* were determined by LC-MS/MS and expressed as mol % of total lipid analyzed. Note that PE is the dominant phospholipid in *D. discoideum*. A y axis break was inserted to highlight minor lipid species such as ceramide (Cer) and PS.

(B) Molecular structures of ester (diacyl) PI (34:1) and ether (alkyl-acyl) PI (O-34:1). (C) Quantification of the distribution of alkyl-acyl species (blue) and diacyl species (gray) within each phospholipid class.

(D) Lipid molecular species composition within each phospholipid class. Shown are the seven most abundant species of each category, except for PS and LPI where only six lipid species were detected. Lipids were quantified as mol % of total lipids analyzed, except for LPI. LPI was quantified as % of total signal due to the absence of an LPI standard. *D. discoideum* was grown for six days in SIH (defined) medium prior to lipid extraction. Lipids were extracted following Folch et al.[40] Data are means ± SD (n = 3).

structure (with the "O" indicating ether linkage of one carbon chain to the glycerol).[24] Strikingly, this also accounts for all other *D. discoideum* phospholipids, except for PC and PG, in which diacyl bonds are more abundant (Figure 2C). In addition, we found that the composition of PI species was highly similar to that reported by a previous study[24] (Figure 2D). In the same study, Clark et al. reported that PI (O-34:1) is comprised of an ether-linked C16:0 fatty acid at its *sn*-1 position. This is consistent with the fact that in our hands lysophosphatidyl-inositol (LPI) (O-16:0) is the most abundant LPI species (Figure 2D).

We conclude that PE is the most abundant phospholipid in *D. discoideum* and that the majority of *D. discoideum* phospholipids are ether lipids that contain alkyl-acyl bonds.

D. discoideum produces phosphoinositol-containing sphingolipids

To identify complex sphingolipids in *D. discoideum* by lipidomics, we used a lipid extraction protocol optimized for the isolation of complex sphingolipids.[41] In brief, total lipids were extracted and subjected to alkaline hydrolysis to deacylate the phospholipids and hence eliminate

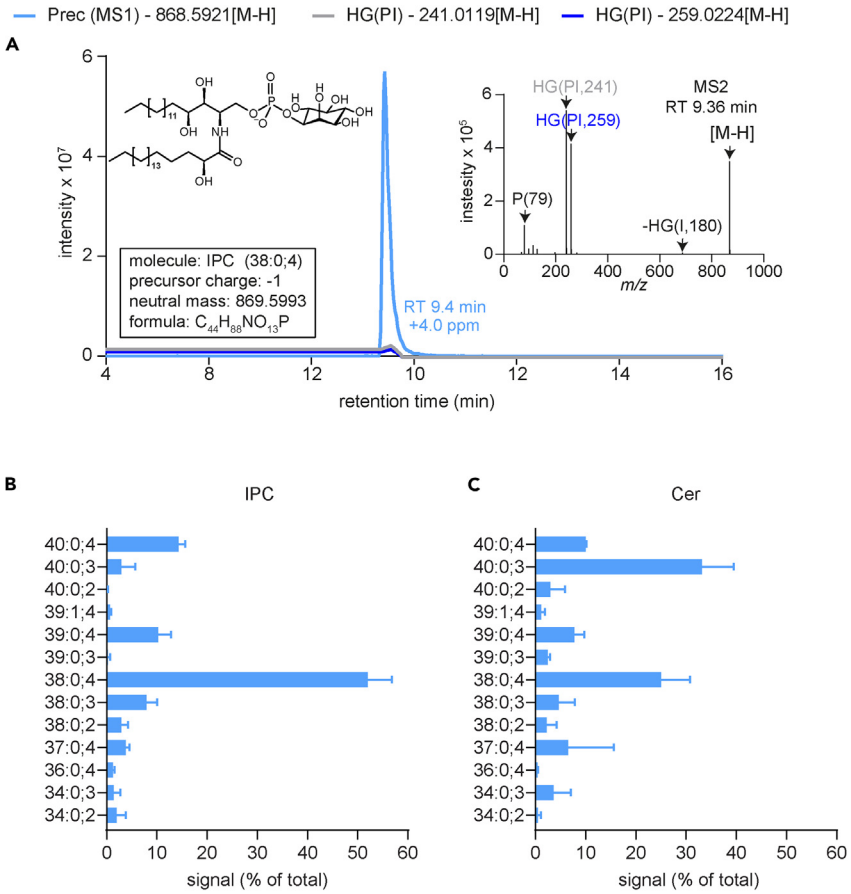

Figure 3. Profiling of IPC and ceramide (Cer) species in *D. discoideum*

(A) Detection of IPC (38:0; 4) by LC-MS/MS. The inset shows the product ion fragmentation of IPC (38:0; 4) at RT 9.36 min.

(B) LC-MS/MS analysis of the main IPC species in *D. discoideum*.

(C) LC-MS/MS analysis of the Cer species in *D. discoideum* that correspond to the IPC species shown in (B) with respect to chain length, hydroxylation status and saturation level. *D. discoideum* was grown in HL5c (complex) medium and then subjected to total lipid extraction according to Sullards et al.[41] The peak area of the precursor ions ([M-H]) from each IPC and Cer species was quantified and normalized with the total peak area from all IPC/Cer species using Skyline. Data are means ± SD (n = 3). HG: head group.

isobaric overlaps between sphingolipids and phospholipids. The efficiency of this method is reflected by the absence of PI (O-34:1) after alkaline hydrolysis (Figure S1). Consequently, this protocol enabled the detection of various species of IPC, with IPC (38:0; 4) being the most abundant IPC species in *D. discoideum* (Figures 3A and 3B). Briefly, "38:0" means that there are 38 carbon atoms in total and no double bonds ("0" unsaturation) in the hydrocarbon chain. "4" indicates that there are four hydroxyl (OH) groups, which might affect the polarity, reactivity, and molecular interactions of the lipid.

The identity of IPC (38:0; 4) was supported by the presence of MS2 fragments (product ions) characteristic for IPC (inositol-1, 2-cyclic phosphate anion and inositol monophosphate anion at m/z 241 and 259, respectively) (Figure 3A, inset). In addition, the product ion at $[M\text{-}H\text{-}180]^-$ represents the loss of the inositol residue and corroborates the claim that the lipid described in Figure 3A is indeed IPC. However, using our current approach, we were not able to conclusively resolve the length of the N-linked acyl chain and LCB from the IPC (38:0; 4) peaks. We therefore analyzed the product ion fragmentation of Cer (38:0; 4), which is presumably the precursor of IPC (38:0; 4) (Figure S2A). The product ions representing LCB (18:0; 3) and LCB (20:0; 3) were both detected in the precursor peak of Cer (38:0; 4) (Figure S2B). However, the intensity of LCB (18:0; 3) was much higher than the one of LCB (20:0; 3). This suggests that Cer (18:0; 3/20:0; 1) constitutes the major proportion of Cer (38:0; 4), while Cer (20:0; 3/18:0; 1) accounts for the minority fraction. From this we infer that the most abundant IPC species in *D. discoideum* is IPC (18:0; 3/20:0; 1).

Besides IPC (38:0; 4) (~52% of total IPC), *D. discoideum* contains various other IPC species, of which the most abundant are IPC (40:0; 4, ~14.3%), IPC (39:0; 4, ~10.3%), and IPC (38:0; 3, ~8.0%; Figure 3B, Table S2). The most abundant ceramide species are Cer (40:0; 3) (~35.9% of total ceramide species), followed by Cer (38:0; 4) (~27.3%), Cer (40:0; 4) (~11.0%), and Cer (39:0; 4) (~8.5%; Figure 3C). This indicates that, like in fungi and plants, complex sphingolipids in *D. discoideum* are mainly based on "phytoceramides" that contain three or more hydroxyl groups. Our analysis also revealed the presence of minor amounts of unsaturated IPC and Cer species as well as odd chain IPCs and Cers (Figures 3B and 3C).

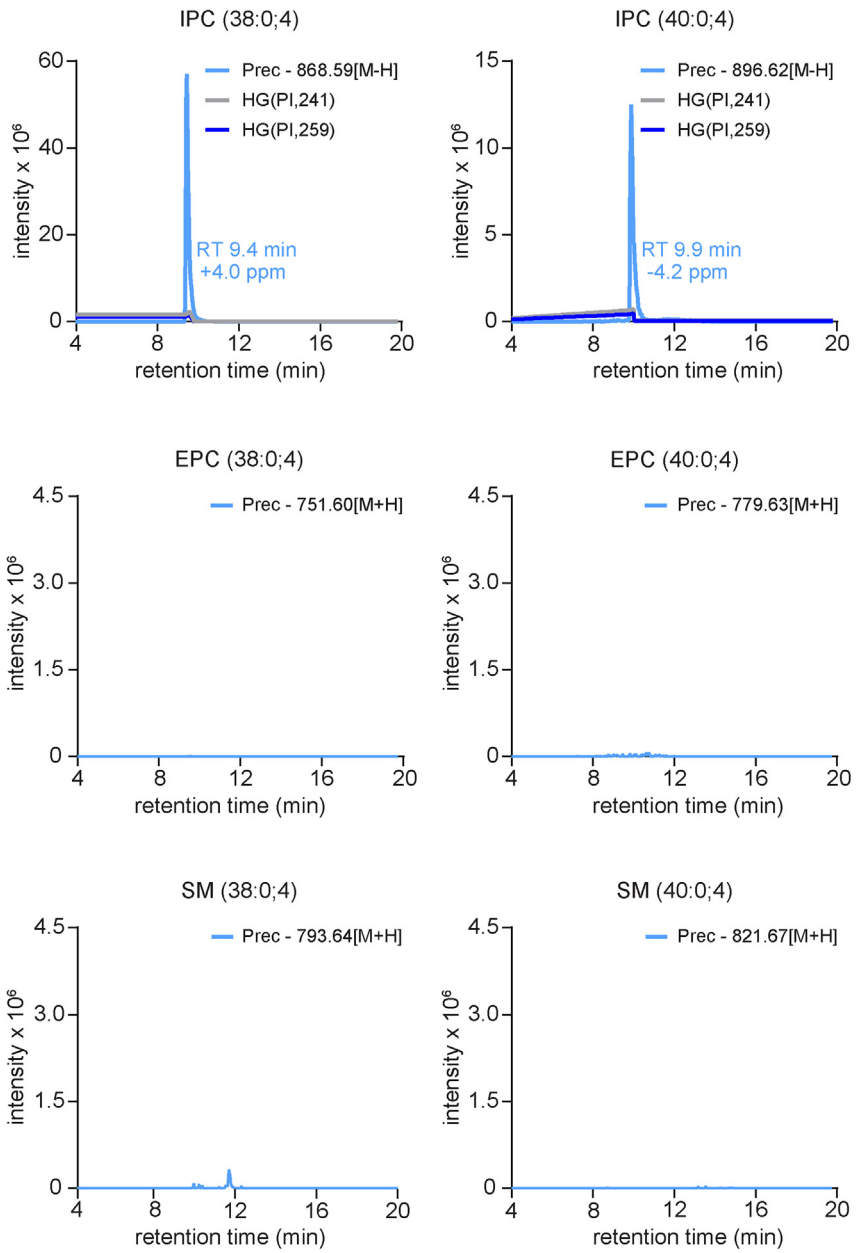

Figure 4. *D. discoideum* exclusively produces inositol-containing phosphosphingolipids

Detection of IPC (38:0; 4) and IPC (40:0; 4) but not their SM or EPC counterparts by LC-MS/MS analysis in alkaline-treated lipid extracts from *D. discoideum*. *D. discoideum* was grown in HL5c (complex) medium. Lipids were extracted following Sullards et al.[41] Data shown are representative of three independent experiments (n = 3). HG: head group.

Given that *D. discoideum* contains more PE and PC than PI (Figure 2A), we also analyzed the alkaline-hydrolyzed *D. discoideum* lipid extracts for the presence of EPC or SM species. However, we did not detect any ethanolamine or choline-containing counterparts of the most abundant IPC species (Figures 4 and S3).

From this we conclude that, analogous to plants and yeast, *D. discoideum* synthesizes IPC. We next set out to identify the corresponding IPC synthase.

A bioinformatics-based search for IPC synthases in *D. discoideum*

As we were not able to identify clear homologs of IPC synthases in *D. discoideum*, we pursued a bioinformatics and functional cloning strategy to identify the IPC synthase(s) in *D. discoideum*. A similar strategy previously led to identification of the human SM synthases SMS1 and

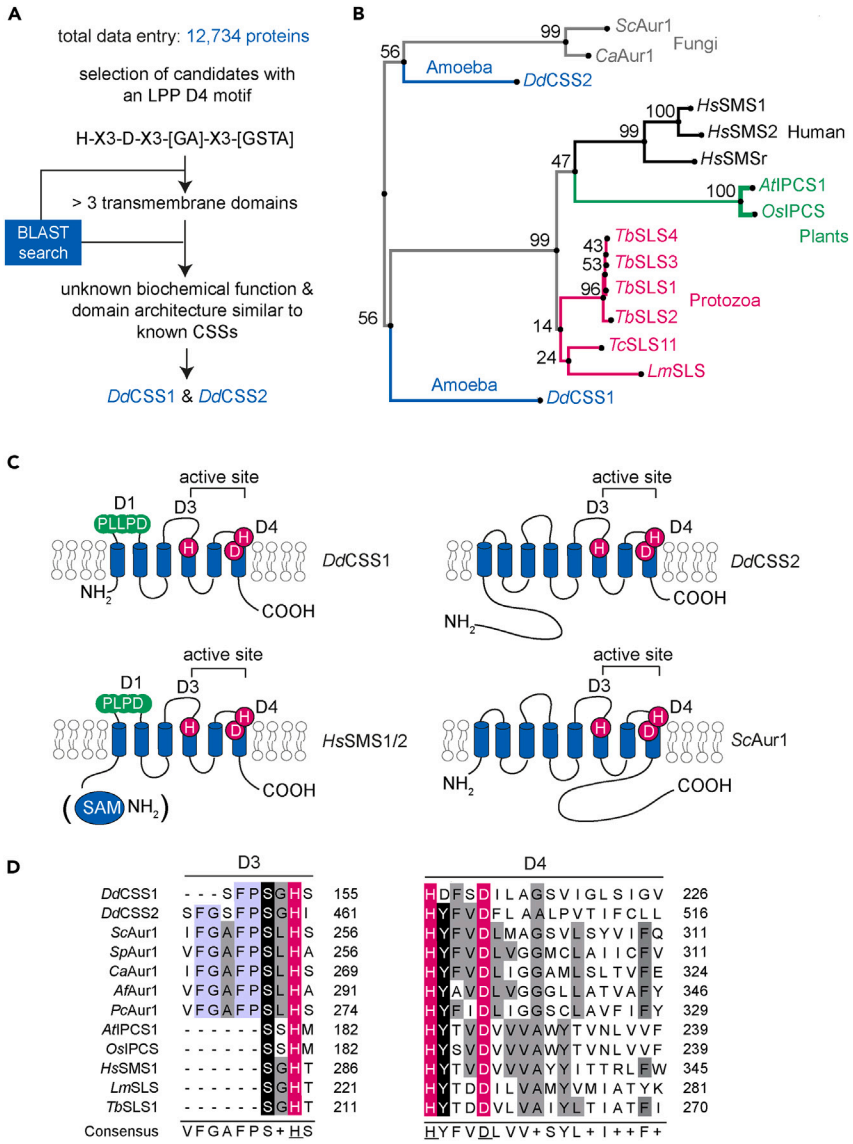

Figure 5. Selection and phylogenetic analysis of candidate IPC synthases in *D. discoideum*

(A) Search of the *D. discoideum* proteome for polytopic membrane proteins that contain the LPP-like sequence motif H-X3-D-X3-[GA]-X3-[GSTA] and meet additional selection criteria as indicated yielded two candidate complex sphingolipid synthases (CSS): *Dd*CSS1 (dictybase: DDB_G0284367) and *Dd*CSS2 (dictybase: DDB_G0268928).

(B) Phylogenetic tree of *Dd*CSS1, *Dd*CSS2, and IPC/SM synthases from different species: *Sc*Aur1 from *Saccharomyces cerevisiae* (UniProt: P36107); *Ca*Aur1 from *Candida albicans* (UniProt: O13332); *At*IPCS1 (UniProt: Q9M325) from *Arabidopsis thaliana*; *Os*IPCS1 from *Oryza sativa* (UniProt: Q5N7A7); *Hs*SMS1, *Hs*SMS2 and *Hs*SMSr (UniProt: Q86VZ5, Q8NHU3, and Q96LT4) from *Homo sapiens*; *Lm*SLS (UniProt: E9AFX2) from *Leishmania*; *Tb*SLS1-4 (UniProt: Q38E54, Q38E56, Q38E53, and Q38E55) from *Trypanosoma brucei; Tc*SLS11 from *Trypanosoma cruzi* (UniProt: Q4E4I4). Protein sequences were aligned with MAFFT (https://mafft.cbrc.jp) using the G-INS-i strategy, unalignlevel 0.0 and "try to align gappy regions away" to generate a phylogenetic tree in phylo.ilo using NJ conserved sites and the JTT substitution model. Numbers on the branches indicate bootstrap support for nodes from 100 bootstrap replicates.

(C) Membrane topology of *Dd*CSS1 and *Dd*CSS2 reconstructed by AlphaFold (https://alphafold.ebi.ac.uk/)(Figure S4C).

(D) Alignment of D3 and D4 sequence motifs in *Dd*CSS1, *Dd*CSS2, and known IPC/SM synthases from different organisms. *Sp*Aur1 (Uniprot: Q10142) from *Schizosaccharomyces pombe*; *Af*Aur1 (UniProt: Q9Y745) from *Aspergillus fumigatus*; *Pc*Aur1 (UniProt: Q9Y745) from *Pneumocystis carinii* (UniProt: Q6AHV1). Alignment was performed with Jalview workbench[42] using the in-built MAFFT alignment option (E-INS-i). Identical residues are shaded in black, conservative residue substitutions are shaded in gray and conserved residues that are part of the catalytic triad are shaded in magenta. Residues conserved among fungal IPC synthases, *Dd*CSS1 and *Dd*CSS2 are shaded in blue.

SMS2.[23] As outlined in Figure 5A, the selection criteria for candidate IPC synthases in *D. discoideum* are: (1) presence of a short sequence motif (H-X3-D-X3-[GA]-X3-[GSTA]) that includes the residues of the catalytic triad shared among all known LPPs and complex sphingolipid synthases (CSSs), including human SMS1/2 and the yeast IPC synthase *Sc*Aur1p; (2) presence of multiple (>3) transmembrane domains (TMDs) given that all known CSSs have six to eight predicted TMDs; (3) biochemical function should be unknown; and (4) the domain architecture should be similar to known CSSs. Of the 12,734 protein sequences analyzed, two met all four selection criteria and therefore qualified as candidate *D. discoideum* IPC synthases, which we designated *Dd*CSS1 and *Dd*CSS2 (Figure 5A). A phylogenetic analysis of CSS sequences from humans, fungi, parasites, plants, and *D. discoideum* revealed that *Dd*CSS1 is more closely related to human SMS and IPCS from plants and protozoa, while *Dd*CSS2 is more closely related to fungal IPC synthases (Figure 5B).

Sequence analysis of *Dd*CSS1 and *Dd*CSS2 revealed two conserved sequence motifs which correspond to the D3 and D4 motifs in human SMS1/2.[23] The D3 (C-G-D-X3-S-G-H-T) and D4 (H-Y-T-X-D-V-X3-Y-X6-F-X2-Y-H) motifs are similar to the C2 and C3 motifs in LPPs[43] and include the histidine and aspartate residues (magenta) that form the catalytic triad mediating the nucleophilic attack on the lipid phosphate ester bond (Figures 5C and 5D).[44] Unlike *Dd*CSS2, *Dd*CSS1 contains a D1 (P-L-P-D)-like motif ("P-L-L-P-D") in its first exoplasmic loop (Figures 5C and S4A) that is also present in human SMS1/2[23] and protozoan IPC synthases.[45] Neither *Dd*CSS1 nor *Dd*CSS2 contains the D2 (R-R-X8-Y-X2-R-X6-T) motif that is typically located in the third transmembrane span of SMS family members. The Aur1-related IPC synthases in fungi contain two unique sequence motifs, here designated IPCS1 (D-h-h-*n*-W-X2-Y-X3-H-X3-P) and IPCS2 (Y-X3-G-X3-G-L-X-R-X-D).[22] The tyrosine residue at position 354 (Y) in the IPCS1 motif and the peptide sequence R-I-D at position 444–446 in the IPCS2 motif might be conserved in *Dd*CSS2 but not in *Dd*CSS1 (Figure S4B).

Using models derived from AlphaFold (Figure S4C), *Dd*CSS1 is predicted to contain six membrane-spanning alpha helices, hence analogous to human SMS1/2 and plant IPCS (Figure 5C). In contrast, *Dd*CSS2 is predicted to contain eight transmembrane domains, analogous to *Sc*Aur1. According to the structures, both N- and C-termini of *Dd*CSS1 and *Dd*CSS2 would be cytosolic while their active site would be positioned on the exoplasmic leaflet (Figure 5C). This is in line with the experimentally established membrane topologies of SMS and LPP family members.[23]

In conclusion, the membrane topology and location of the catalytic triad in *Dd*CSS1 and *Dd*CSS2 indicate that both proteins qualify as candidate CSS. Moreover, *Dd*CSS2 shares additional structural features with IPC synthases in fungi.

*Dd*CSS2 displays IPC synthase activity

To determine whether *D. discoideum* lysates possess IPC activity, we performed an NBD-ceramide turnover assay and used *S. cerevisiae* as control. Interestingly, the addition of PI to the yeast samples resulted in the appearance of a distinct band (Figure 6A). A similar band was observed for *D. discoideum*. This is compelling evidence that *D. discoideum* has both the enzyme and the capacity to make IPC.

Next, to monitor the IPC synthase activity of *D. discoideum* CSS, the mRNAs of *Dd*CSS1 and *Dd*CSS2 were synthesized *in vitro* and translated in a wheat germ extract (WGE) in the presence of unilamellar liposomes prepared from a mixture of PC, PE, and PI (Figure 6B). This approach previously enabled the cell-free production of enzymatically active *Hs*SMS1/2[46] and protozoan IPC synthases.[21] In brief, the cDNAs of *Dd*CSS1 and *Dd*CSS2 were cloned downstream of the Sp6 promoter in pEU Flexi-vector pFLx.[47] A pFLx construct encoding *Hs*SMS2 served as control. To facilitate detection of the cell-free-produced proteins, a V5-epitope was introduced at their C-termini. As shown in Figure 6C (top panel), cell-free translation of *Dd*CSS1/2 and *Hs*SMS2 mRNA in the presence of liposomes in each case yielded a V5-tagged protein of the expected size. No such protein was detected when translation was performed in the absence of mRNA. Next, proteoliposomes were incubated with the fluorescent short-chain (C6) Cer analog NBD-Cer and the formation of complex NBD-labeled sphingolipids was monitored by TLC. As expected, proteoliposomes containing *Hs*SMS2 supported production of NBD-SM (Figure 6C, bottom panel; Figure S5A). In contrast, proteoliposomes containing *Dd*CSS1 did not yield any obvious NBD-labeled reaction product. However, the reaction with *Dd*CSS2 proteoliposomes yielded an NBD-labeled product with a retention value distinct from NBD-SM but similar to that of NBD-IPC (Figure 6C, bottom panel; Figure S5A). Importantly, omission of PI from *Dd*CSS2 proteoliposomes abolished production of the NBD-labeled lipid while omission of PC or PE did not (Figure 6D, bottom panel; Figure S5B-C). Conversely, omission of PC from *Hs*SMS2 proteoliposomes diminished but did not entirely eliminate production of NBD-SM, presumably because the WGE contains residual amounts of PC (Figure S5D). From this we conclude that *Dd*CSS2 possesses IPC synthase activity. The activity of *Dd*CSS1 remains to be established.

To address whether *Dd*CSS2 is responsible for IPC production in *D. discoideum*, we set out to generate a *css2* knockout strain. Unfortunately, all our efforts toward this end were unsuccessful. In addition, the extensive restriction-enzyme-mediated insertional mutagenesis (REMI) library of *D. discoideum*[48] does not contain any *css2* mutants. This suggests that, analogous to the IPCS-encoding gene in yeast,[49] *Dd*CSS2 is an essential gene.

The cyclic depsipeptide antibiotic aureobasidin A (AbA) is a potent inhibitor of IPC synthase from fungi.[50,51] Indeed, addition of AbA (50 μM) to yeast lysates co-incubated with NBD-Cer and externally added PI effectively blocked the formation of NBD-IPC (Figure S6A). Moreover, the NBD-IPC synthase activity of cell-free produced *Dd*CSS2 was resistant to even high levels of AbA (500 μM). Also, prolonged treatment of *D. discoideum* with AbA had no impact on steady state IPC levels (Figure S6B).

In sum, our results indicate that *Dd*CSS2 functions as an IPC synthase that lacks the AbA sensitivity typical for IPC synthases from fungi.

*Dd*CSS2 localizes to the Golgi apparatus and the contractile vacuole

Previous work revealed that the enzymes responsible for bulk production of IPC, EPC, and SM typically localize to the Golgi complex.[11,16,23] To determine the subcellular localization of *Dd*CSS2, we tagged *Dd*CSS2 with mCherry at either its N- (mCherry-CSS2) or C-terminus

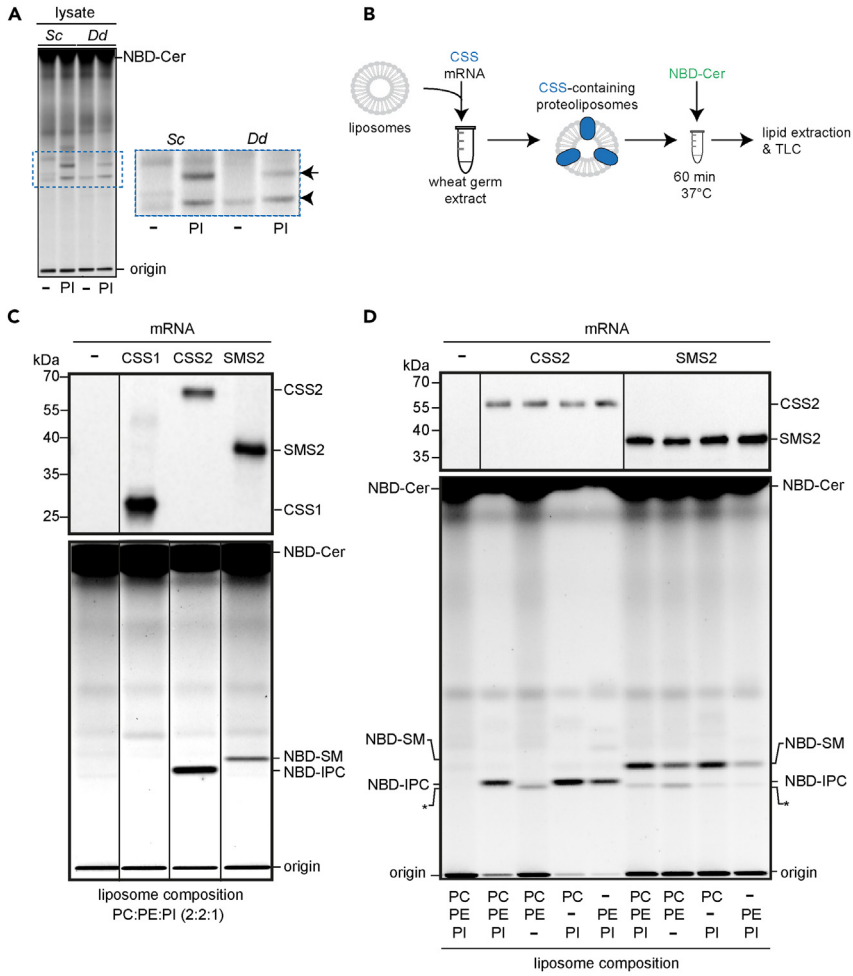

Figure 6. Cell free-expression and functional analysis of *Dd*CSS1 and *Dd*CSS2

(A) *D. discoideum* lysates possess PI:Cer cholinephosphotransferase activity. NBD-Cer turnover assay with lysates of *D. discoideum* and yeast. Lysates were treated with PI as indicated. Arrow points to the potential band of IPC-NBD, while the arrowhead indicates an unidentified band.

(B) Schematic outline of the wheat germ-based cell-free translation of CSS mRNA. Unless indicated otherwise, translation reactions were carried out in the presence of liposomes with defined lipid compositions. The resulting proteoliposomes were incubated with NBD-Cer and NBD-labeled reaction products were analyzed by TLC.

(C) Top panel: translation reactions with or without mRNA encoding V5-tagged *Dd*CSS1, *Dd*CSS2, and *Hs*SMS2 carried out in the presence of liposomes with the indicated lipid composition were subjected to western blot analysis using an anti-V5 antibody. Bottom panel: TLC analysis of reaction products formed when *Dd*CSS1, *Dd*CSS2, and *Hs*SMS2 produced in the presence of liposomes containing PC:PE:PI (2:2:1) were incubated with NBD-Cer for 60 min at 37°C.

(D) Top panel: translation reactions with or without mRNA encoding V5-tagged *Dd*CSS2 or *Hs*SMS2 carried out in the presence of liposomes with the indicated lipid composition were subjected to western blot analysis using an anti-V5 antibody. Bottom panel: TLC analysis of reaction products formed when *Dd*CSS2 and *Hs*SMS2 produced in the presence of liposomes with the indicated lipid composition were incubated with NBD-Cer for 60 min at 37°C. Migration of an unidentified fluorescent lipid that was present in reactions irrespective of the presence of *Dd*CSS2 or *Hs*SMS2 and is probably background from the WGE is marked by an asterisk.

(CSS2-mCherry). Expression of the tagged proteins in *D. discoideum* was confirmed by western blotting (Figure S7A). Imaging of these strains by confocal laser scanning microscopy (CLSM) revealed that both CSS2-mCherry and mCherry-CSS2 displayed a partial co-localization with ZntD-GFP, a zinc transporter present in the juxtanuclear region that is characteristic for the Golgi complex/recycling endosomes in *D. discoideum*[52] (Figures 7A and 7B, arrows). CSS2 localization at the Golgi complex became very clear when the z-slices were combined to a 3D-model (Figures 7C and 7D) and was confirmed by immunofluorescence (IF) using the Golgi marker AK426 antibody (Figures 7E and 7F).[53–55] In contrast, we did not observe any co-localization of mCherry-CSS2 or CSS2-mCherry with the ER marker protein disulfide isomerase (PDI) (Figure S7B) or with the mitochondrial marker porin A (PorA) (Figure S7C). On the other hand, both fusion proteins were present at membrane structures resembling bladders of the CV system prior water expulsion (Figure 7Ci and Di, arrowheads), as well as on vesicle-like structures that became only visible during live imaging and were more prevalent in CSS2-mCherry expressing cells (Figure S8).

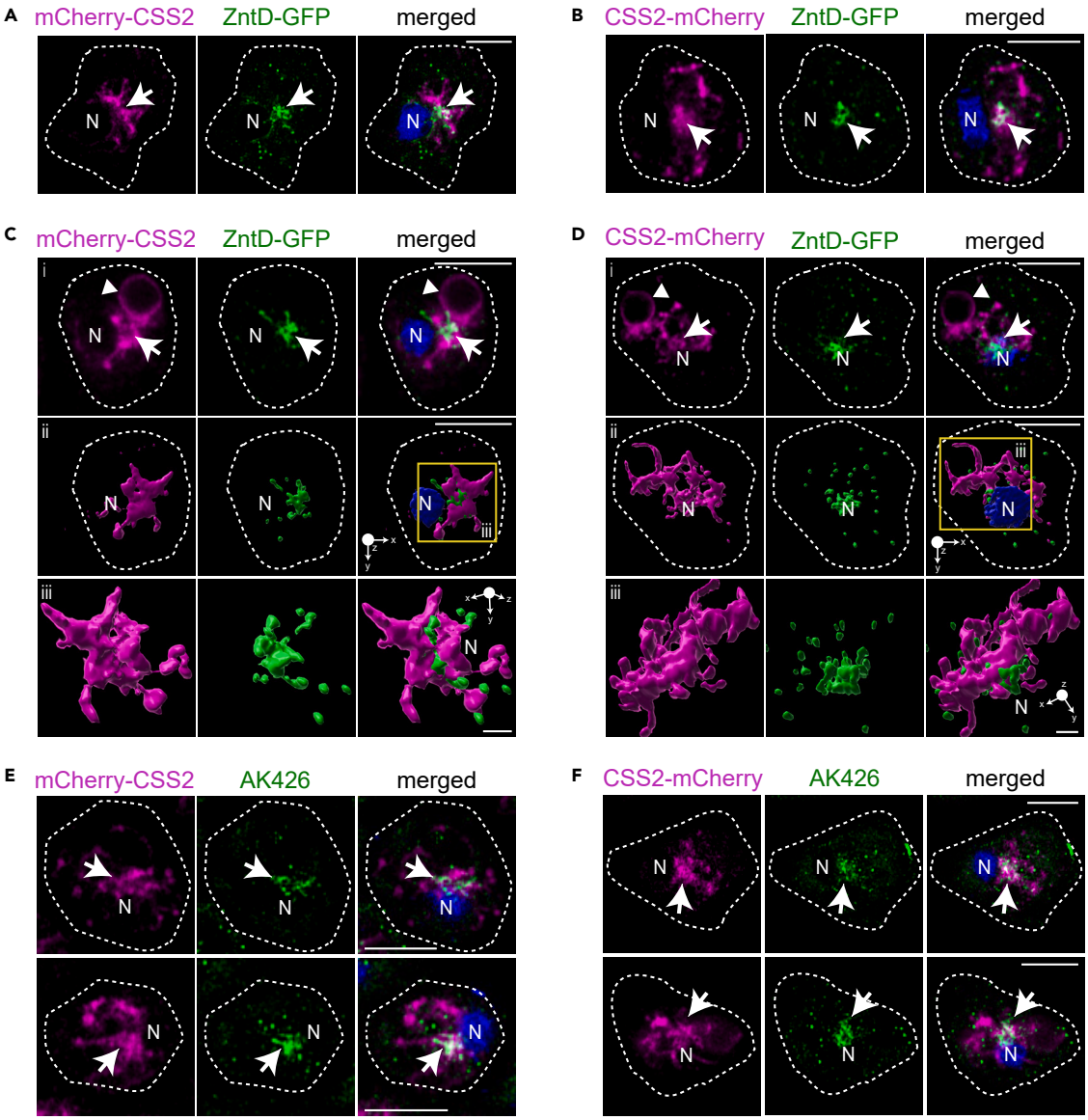

Figure 7. *DdCSS2* partially accumulates at the Golgi complex in *D. discoideum*

(A and B) CSS2-mCherry as well as mCherry-CSS2 co-localize with ZntD-GFP, a zinc transporter that is located at the Golgi apparatus/recycling endosomes.

(C and D) 3D-models (ii, iii) generated from cells shown in panel i highlight the localization of CSS2 at the Golgi complex.

(E and F) CSS2-mCherry as well as mCherry-CSS2 co-localize with the Golgi marker AK426.[53] Cells were fixed with MeOH, stained with DAPI and the AK426 antibody and imaged using confocal laser scanning microscopy (CLSM). Arrowheads point to potential CV bladders. Arrows indicate co-localization. N: nucleus. Scale bars, 5 μm; 1 μm (iii).

To analyze the localization of *Dd*CSS2 on CV bladders, cells expressing the mCherry-tagged proteins were fed with latex beads, fixed and then stained with an antibody against VatA, a subunit of the vATPase that is present in both lysosomes and membranes of the CV network (Figures 8A, 8B, and 8Ci–8Di, arrowheads).[56] To distinguish between the CV and lysosomes, cells were additionally stained for p80, a copper transporter that resides in all endosomes in *D. discoideum* and accumulates on latex beads upon phagosomal maturation (i.e., lysosomes: p80-low; post-lysosomes: p80-high).[57] Indeed, the presence of both mCherry-tagged CSS2 versions at VatA-positive, p80-negative compartments (Figures 8Ci–8Di, arrowheads) and their absence at VatA-positive, bead-containing phagosomes (BCPs) (Figures 8A and 8B, asterisks) suggests that *Dd*CSS2 is confined to the CV and does not reside in lysosomes. This was particularly evident in 3D-models of CV bladders, which form shortly before the water discharge and have a morphologically very typical structure (Figures 8C and 8D). In addition, we did not observe any co-localization of CSS2-mCherry or mCherry-CSS2 on vacuolin-positive BCPs, indicating that *Dd*CSS2 is not a phagosomal protein (Figures 8E and 8F).

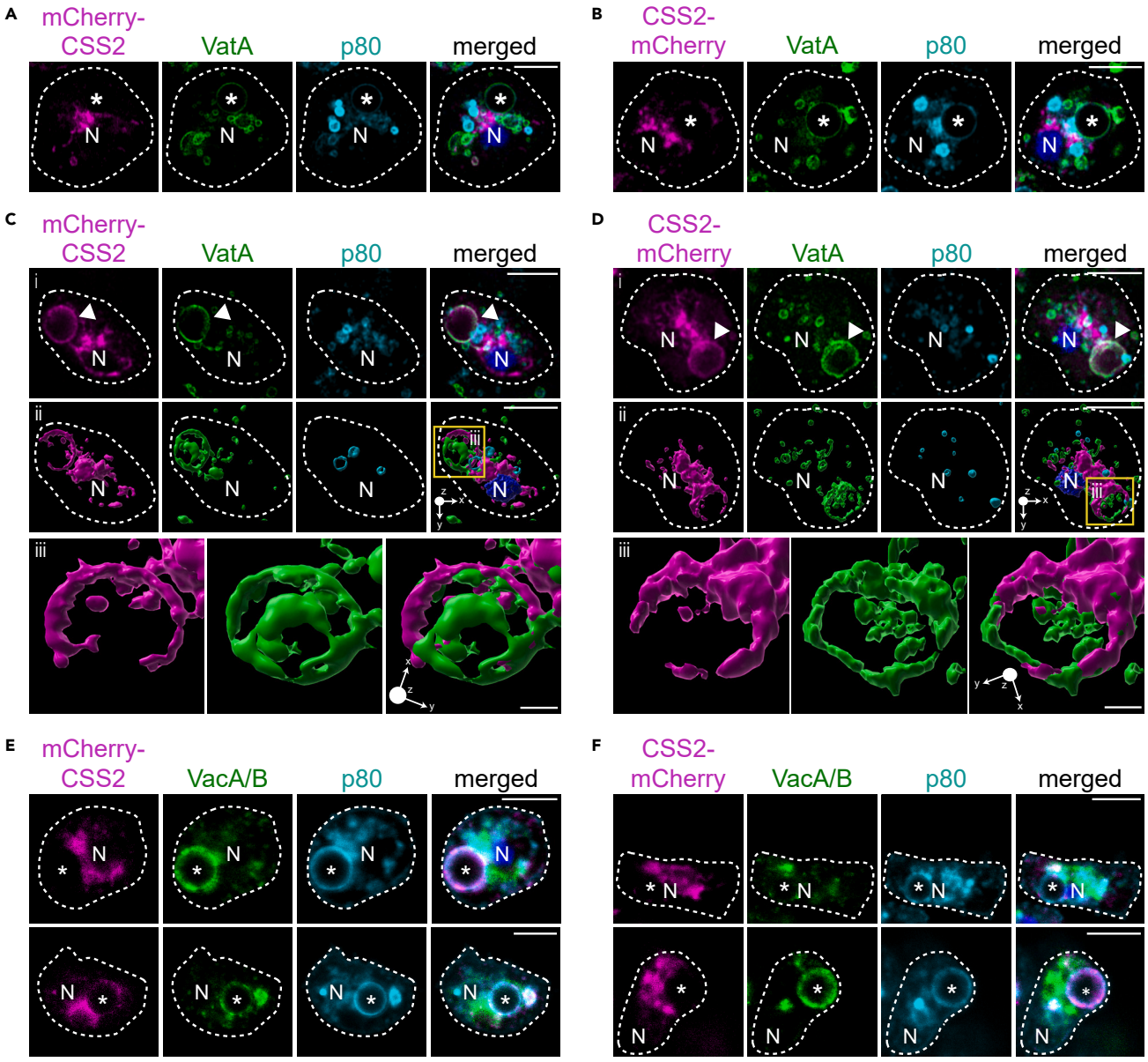

Figure 8. *DdCSS2* partially accumulates at the contractile vacuole (CV) in *D. discoideum*

(A and B) CSS2-mCherry and mCherry-CSS2 do not co-localize with VatA-positive, p80-positive BCPs (i.e., phagosomes).

(C and D) 3D-models (ii, iii) generated from cells shown in panel i highlight the localization of CSS2 at CV (VatA-positive, p80-negative).

(E and F) CSS2-mCherry and mCherry-CSS2 do not accumulate on BCPs. CSS2-mCherry and mCherry-CSS2 expressing cells were incubated with 3 μm latex beads, fixed with MeOH (A–D) or PFA/picric acid (E and F) and stained with either anti-VatA (A–D) or anti-VacA/B (E and F) and anti-p80 antibodies (A–F). Images were generated by CLSM. Asterisks label BCPs. Arrowheads label CSS2-positive CV bladders. N: nucleus. Scale bars, 5 μm; 1 μm (iii).

From this we conclude that the IPC synthase *Dd*CSS2 in *D. discoideum* resides at the Golgi. Moreover, our findings demonstrate an additional localization of the enzyme at the CV.

DISCUSSION

While *D. discoideum* has been extensively used as experimental model in cell and infection biology, information on its sphingolipidome and the underlying sphingolipid biosynthetic pathway has remained scarce.

BLAST searches for homologs of sphingolipid biosynthetic enzymes with LC-MS/MS-based lipid profiling and the functional characterization of cell-free expressed enzymes, we found that *D. discoideum* primarily synthesizes PI-containing sphingolipids with

phytoceramide backbones. Identification of the corresponding IPC synthase, *Dd*CSS2, revealed a polytopic membrane protein that shares multiple sequence motifs with both yeast IPC synthases and human SM synthases. Interestingly, *Dd*CSS2 displays a dual localization in *D. discoideum*, being present in both the Golgi apparatus and the organism's osmoregulatory vacuole.

Our untargeted LC-MS/MS lipidome analyses revealed that, in line with previous studies,[25,58] the phospholipid pool in *D. discoideum* is mostly composed of ether lipids, i.e., lipids with ether-linked acyl-chains that are less abundant in mammals[59,60] and absent in plants or fungi.[61] Similar to *E. coli*[62] and *D. melanogaster*,[63] we found that PE is by far the most abundant phospholipid class in *D. discoideum*. These data are consistent with those reported previously by others.[25,58,64]

Strikingly, analogous to plants and yeast,[65] *D. discoideum* mainly synthesizes IPC species containing a phytoceramide backbone with amide-linked acyl chains of 16–22 carbon atoms in length. Thus, the fatty-acid moieties in IPC species of *D. discoideum* are significantly shorter than those in yeast. While Cer (40:0; 3) is the most abundant Cer in *D. discoideum*, the levels of IPC (40:0; 3) are relatively low. This suggests that the IPC synthase in *D. discoideum* may prefer phytoceramides with α-hydroxylated acyl chains as substrate.

IPC species in *D. discoideum* may undergo further head group modifications such as mannosylation for the production of mannosylinositol phosphorylceramide (MIPC) in yeast or glucuronosylation for the production of glycosylinositol phosphorylceramides (GIPC) in plants. While our lipidome analysis so far did not uncover such IPC derivatives, the *D. discoideum* genome encodes a putative homolog of the plant inositol phosphoryl ceramide glucuronosyl transferase 1 (IPUT1) (dictybase: DDB_G0286945) (Table S1), which transfers a glucuronic acid residue to the IPC head group in *A. thaliana*.[66] Altogether, we conclude that the sphingolipidome of *D. discoideum* is unique and, if any, possesses greater similarities to the sphingolipidomes of *S. cerevisiae* and plants than those of animals.

BLAST searches for homologs of core metabolic enzymes enabled us to partially reconstruct the sphingolipid biosynthetic pathway in *D. discoideum*. However, this strategy did not yield any information on the enzymes responsible for the production of complex sphingolipids. As complementary approach, we searched for polytopic membrane proteins in *D. discoideum* having sequence motifs in common with known IPC and SM synthases, yielding *Dd*CSS1 and *Dd*CSS2. Subsequent analysis of *Dds*CSS1 did not provide any information on its enzymatic activity. However, BLAST searches revealed similarities between *Dd*CSS1 and the yeast diacylglycerol pyrophosphate phosphatase 1 (*Sc*Dpp1), an enzyme that dephosphorylates diacylglycerol pyrophosphate to generate phosphatidate (PA) and subsequently dephosphorylates PA to release diacylglycerol. Whether *Dd*CSS1 mediates dephosphorylation of PA remains to be established.

*Dd*CSS2, on the other hand, qualified as IPC synthase based on the following criteria: (i) cell-free expressed *Dd*CSS2 supports the production of IPC when supplemented with ceramide and PI as head group donor; (ii) *Dd*CSS2 shares sequence motifs containing active site residues with known IPC synthases in plants and yeast; (iii) *Dd*CSS2 is predicted to adopt a membrane topology similar to that of IPC synthases in plants and yeast whereby the active site residues are facing the exoplasmic leaflet, hence the side of the membrane where IPC production is thought to occur; (iv) *Dd*CSS2 localizes to the Golgi apparatus, the organelle previously established as the principle site of IPC production in plants and yeast.[11,23,45,67] Consequently, we propose to rename *Dd*CSS2 as *Dd*IPCS1 for *D. discoideum* IPC synthase 1.

In spite of its close relationship with the yeast IPC synthase *Sc*Aur1, *Dd*IPCS1 displayed resistance to the cyclic depsipeptide antibiotic AbA, which is a potent inhibitor of the yeast enzyme.[18,21,68] Inhibition of *Sc*Aur1 by AbA is dependent on residues 137, 157, and 158,[51,69] which are part of a sequence motif that is not well conserved in *Dd*IPCS1 (Figure S4B, magenta box). AbA was originally isolated from *Aureobasidium pullulans*, a yeast-like fungus found in the natural habitat of *D. discoideum*.[70] Thus, it is conceivable that mutations in *Dd*IPCS1 enabled *D. discoideum* to develop resistance against the antibiotic activity of AbA. Also of note is the dual location of *Dd*IPCS1, which resides in both the Golgi apparatus and the CV. In *D. discoideum* and other free-living organisms, the CV is an osmoregulatory organelle for water expulsion under hypotonic conditions.[71] Water discharge is carried out by a giant kiss-and-run exocytic event. CV discharge may provide an alternative mode to deliver IPC produced by *Dd*IPCS1 to the PM. This may be necessary to sustain the gradient of complex sphingolipids along the secretory pathway, with the highest concentration at the PM.

Whether *Dd*IPCS1 is the sole IPC synthase in *D. discoideum* remains to be established. All our efforts to generate *Dd*IPCS1 knockouts by homologous recombination were unsuccessful, suggesting that *Dd*IPCS1 is essential for *D. discoideum* growth and survival. Similar observations have been made for IPC synthases in *A. thaliana* and *S. cerevisiae*[51,66] while in *T. brucei*, RNAi-mediated knockdown of the entire gene locus encoding *Tb*SLS1-4 is lethal.[72] Future *Dd*IPCS1 knockdown studies should help elucidate the biological roles of IPC production in *D. discoideum* in particular during host-pathogen interactions. Given that *D. discoideum* was exploited by pathogens well before the evolution of mammals, we anticipate that such studies may uncover very fundamental sphingolipid-dependent mechanisms underlying infection.

Limitations of the study

While this study offers fresh insights into the lipidome and the phosphosphingolipid species generated by *D. discoideum*, it has several limitations that should be addressed in future studies. For instance, since there is currently no commercially available IPC standard, lipidomics did not reveal the cellular IPC levels of *D. discoideum*. In addition, cell-free expression and other experiments were performed with C6-NBD-ceramide. This shorter version is more soluble in aqueous solutions ensuring the reliability and reproducibility of enzymatic assays. Future *in vivo* experiments should be performed with the more physiological C18-NBD-ceramide. Moreover, since all experiments deciphering the function of CSS2 were conducted in *in vitro* settings, additional work on role of this enzyme will be carried out in future. To avoid potential errors caused by the bulky mCherry tag, future subcellular localization experiments for CSS2 should be carried out with smaller Halo- or ALFA-tags.

STAR★METHODS

Detailed methods are provided in the online version of this paper and include the following:

- KEY RESOURCES TABLE
- RESOURCE AVAILABILITY
  - Lead contact
  - Materials availability
  - Data and code availability
- EXPERIMENTAL MODEL
  - D. discoideum strains and cell culture
- METHOD DETAILS
  - Lipidomics
  - Preparation of liposomes
  - CFE and CSS activity assay
  - Live fluorescence microscopy
  - Bead phagocytosis and immunofluorescence
  - SDS-PAGE and western blotting
  - Selection and prediction of D. discoideum CSS
- QUANTIFICATION AND STATISTICAL ANALYSIS

SUPPLEMENTAL INFORMATION

Supplemental information can be found online at https://doi.org/10.1016/j.isci.2024.110609.

ACKNOWLEDGMENTS

We greatly acknowledge the integrated Bioimaging facility (iBiOs) at the University of Osnabrück and the advanced light and fluorescence microscopy (AFLM) facility at CSSB and especially Rainer Kurre (iBiOs) and Roland Thünauer (CSSB) for their expertise and friendly support. We thank Thierry Soldati, Dominik Schwudke, and Nicolas Gisch for carefully reading this manuscript and thoughtful suggestions. This work was supported by the Deutsche Forschungsgemeinschaft (SFB1557-P1 to C.B. and SFB1557-P7 to J.C.M.H). The Barisch lab is a member of the SPP2225.

AUTHOR CONTRIBUTIONS

S.A.L. conducted the experiments, analyzed the data and wrote the manuscript. A.-C.M. conducted experiments, analyzed the data and edited the manuscript for the revision, M.K., E.U., and S.E. conducted experiments. F.F. and S.W. conceived experiments. J.C.M.H. conceived experiments and amended the manuscript. C.B. analyzed data, wrote, and amended the manuscript and secured the funding.

DECLARATION OF INTERESTS

The authors declare no competing interests.

Received: January 9, 2024
Revised: June 12, 2024
Accepted: July 26, 2024
Published: July 30, 2024

REFERENCES

1. Sokoya, T., Parolek, J., Foged, M.M., Danylchuk, D.I., Bozan, M., Sarkar, B., Hilderink, A., Philippi, M., Botto, L.D., Terhal, P.A., et al. (2022). Pathogenic variants of sphingomyelin synthase SMS2 disrupt lipid landscapes in the secretory pathway. Elife *11*, e79278.
2. van Meer, G., Voelker, D.R., and Feigenson, G.W. (2008). Membrane lipids: where they are and how they behave. Nat. Rev. Mol. Cell Biol. *9*, 112–124.
3. Lingwood, D., and Simons, K. (2010). Lipid rafts as a membrane-organizing principle. Science *327*, 46–50.
4. Slotte, J.P. (2013). Biological functions of sphingomyelins. Prog. Lipid Res. *52*, 424–437.
5. Hannun, Y.A., and Obeid, L.M. (2018). Sphingolipids and their metabolism in physiology and disease. Nat. Rev. Mol. Cell Biol. *19*, 175–191.
6. Maceyka, M., and Spiegel, S. (2014). Sphingolipid metabolites in inflammatory disease. Nature *510*, 58–67.
7. Michel, C., van Echten-Deckert, G., Rother, J., Sandhoff, K., Wang, E., and Merrill, A.H., Jr. (1997). Characterization of ceramide synthesis. A dihydroceramide desaturase introduces the 4,5-trans-double bond of sphingosine at the level of dihydroceramide. J. Biol. Chem. *272*, 22432–22437.
8. Dickson, R.C. (1998). Sphingolipid functions in Saccharomyces cerevisiae: comparison to mammals. Annu. Rev. Biochem. *67*, 27–48.
9. Zelnik, I.D., Rozman, B., Rosenfeld-Gur, E., Ben-Dor, S., and Futerman, A.H. (2019). A Stroll Down the CerS Lane. Adv. Exp. Med. Biol. *1159*, 49–63.
10. Markham, J.E., Lynch, D.V., Napier, J.A., Dunn, T.M., and Cahoon, E.B. (2013). Plant sphingolipids: function follows form. Curr. Opin. Plant Biol. *16*, 350–357.
11. Levine, T.P., Wiggins, C.A., and Munro, S. (2000). Inositol phosphorylceramide synthase

is located in the Golgi apparatus of Saccharomyces cerevisiae. Mol. Biol. Cell *11*, 2267–2281.
12. Holthuis, J.C., Pomorski, T., Raggers, R.J., Sprong, H., and Van Meer, G. (2001). The organizing potential of sphingolipids in intracellular membrane transport. Physiol. Rev. *81*, 1689–1723.
13. Ullman, M.D., and Radin, N.S. (1974). The enzymatic formation of sphingomyelin from ceramide and lecithin in mouse liver. J. Biol. Chem. *249*, 1506–1512.
14. Voelker, D.R., and Kennedy, E.P. (1982). Cellular and enzymic synthesis of sphingomyelin. Biochemistry *21*, 2753–2759.
15. Satouchi, K., Hirano, K., Sakaguchi, M., Takehara, H., and Matsuura, F. (1993). Phospholipids from the free-living nematode Caenorhabditis elegans. Lipids *28*, 837–840.
16. Vacaru, A.M., van den Dikkenberg, J., Ternes, P., and Holthuis, J.C.M. (2013). Ceramide phosphoethanolamine biosynthesis in Drosophila is mediated by a unique ethanolamine phosphotransferase in the Golgi lumen. J. Biol. Chem. *288*, 11520–11530.
17. Mina, J.G.M., and Denny, P.W. (2018). Everybody needs sphingolipids, right! Mining for new drug targets in protozoan sphingolipid biosynthesis. Parasitology *145*, 134–147.
18. Nagiec, M.M., Nagiec, E.E., Baltisberger, J.A., Wells, G.B., Lester, R.L., and Dickson, R.C. (1997). Sphingolipid synthesis as a target for antifungal drugs. Complementation of the inositol phosphorylceramide synthase defect in a mutant strain of Saccharomyces cerevisiae by the AUR1 gene. J. Biol. Chem. *272*, 9809–9817.
19. Malgat, M., Maurice, A., and Baraud, J. (1986). Sphingomyelin and ceramide-phosphoethanolamine synthesis by microsomes and plasma membranes from rat liver and brain. J. Lipid Res. *27*, 251–260.
20. Rietveld, A., Neutz, S., Simons, K., and Eaton, S. (1999). Association of Sterol- and Glycosylphosphatidylinositol-linked Proteins with Drosophila Raft Lipid Microdomains. J. Biol. Chem. *274*, 12049–12054.
21. Sevova, E.S., Goren, M.A., Schwartz, K.J., Hsu, F.F., Turk, J., Fox, B.G., and Bangs, J.D. (2010). Cell-free synthesis and functional characterization of sphingolipid synthases from parasitic trypanosomatid protozoa. J. Biol. Chem. *285*, 20580–20587.
22. Heidler, S.A., and Radding, J.A. (2000). Inositol phosphoryl transferases from human pathogenic fungi. Biochim. Biophys. Acta *1500*, 147–152.
23. Huitema, K., van den Dikkenberg, J., Brouwers, J.F.H.M., and Holthuis, J.C.M. (2004). Identification of a family of animal sphingomyelin synthases. Embo j *23*, 33–44.
24. Clark, J., Kay, R.R., Kielkowska, A., Niewczas, I., Fets, L., Oxley, D., Stephens, L.R., and Hawkins, P.T. (2014). Dictyostelium uses ether-linked inositol phospholipids for intracellular signalling. Embo j *33*, 2188–2200.
25. Kappelt, F., Du Ma, X., Abou Hasna, B., Kornke, J.M., and Maniak, M. (2020). Phospholipids containing ether-bound hydrocarbon-chains are essential for efficient phagocytosis and neutral lipids of the ester-type perturb development in Dictyostelium. Biol. Open *9*, bio052126.
26. Barisch, C., and Soldati, T. (2017). Mycobacterium marinum Degrades Both Triacylglycerols and Phospholipids from Its Dictyostelium Host to Synthesise Its Own Triacylglycerols and Generate Lipid Inclusions. PLoS Pathog. *13*, e1006095.
27. Barisch, C., Paschke, P., Hagedorn, M., Maniak, M., and Soldati, T. (2015). Lipid droplet dynamics at early stages of Mycobacterium marinum infection in Dictyostelium. Cell Microbiol. *17*, 1332–1349.
28. Eichinger, L., Pachebat, J.A., Glöckner, G., Rajandream, M.A., Sucgang, R., Berriman, M., Song, J., Olsen, R., Szafranski, K., Xu, Q., et al. (2005). The genome of the social amoeba Dictyostelium discoideum. Nature *435*, 43–57.
29. Mamode Cassim, A., Grison, M., Ito, Y., Simon-Plas, F., Mongrand, S., and Boutté, Y. (2020). Sphingolipids in plants: a guidebook on their function in membrane architecture, cellular processes, and environmental or developmental responses. FEBS Lett. *594*, 3719–3738.
30. Schäfer, J.-H., Körner, C., Esch, B.M., Limar, S., Parey, K., Walter, S., Januliene, D., Moeller, A., and Fröhlich, F. (2023). Structure of the ceramide-bound SPOTS complex. Nat Commun. *14*, 6196.
31. Snider, J.M., Luberto, C., and Hannun, Y.A. (2019). Approaches for probing and evaluating mammalian sphingolipid metabolism. Anal. Biochem. *575*, 70–86.
32. Cingolani, F., Futerman, A.H., and Casas, J. (2016). Ceramide synthases in biomedical research. Chem. Phys. Lipids *197*, 25–32.
33. Kageyama-Yahara, N., and Riezman, H. (2006). Transmembrane topology of ceramide synthase in yeast. Biochem. J. *398*, 585–593.
34. Luttgeharm, K.D., Chen, M., Mehra, A., Cahoon, R.E., Markham, J.E., and Cahoon, E.B. (2015). Overexpression of Arabidopsis Ceramide Synthases Differentially Affects Growth. Plant Physiol. *169*, 1108–1117.
35. Pathak, D., Mehendale, N., Singh, S., Mallik, R., and Kamat, S.S. (2018). Lipidomics Suggests a New Role for Ceramide Synthase in Phagocytosis. ACS Chem. Biol. *13*, 2280–2287.
36. Rahmaniyan, M., Curley, R.W., Jr., Obeid, L.M., Hannun, Y.A., and Kraveka, J.M. (2011). Identification of dihydroceramide desaturase as a direct in vitro target for fenretinide. J. Biol. Chem. *286*, 24754–24764.
37. Michaelson, L.V., Zäuner, S., Markham, J.E., Haslam, R.P., Desikan, R., Mugford, S., Albrecht, S., Warnecke, D., Sperling, P., Heinz, E., and Napier, J.A. (2009). Functional characterization of a higher plant sphingolipid Delta4-desaturase: defining the role of sphingosine and sphingosine-1-phosphate in Arabidopsis. Plant Physiol. *149*, 487–498.
38. Chen, M., Markham, J.E., and Cahoon, E.B. (2012). Sphingolipid Δ8 unsaturation is important for glucosylceramide biosynthesis and low-temperature performance in Arabidopsis. Plant J. *69*, 769–781.
39. Eisenberg, T., and Büttner, S. (2014). Lipids and cell death in yeast. FEMS Yeast Res. *14*, 179–197.
40. Folch, J., Lees, M., and Sloane Stanley, G.H. (1957). A simple method for the isolation and purification of total lipides from animal tissues. J. Biol. Chem. *226*, 497–509.
41. Sullards, M.C., Liu, Y., Chen, Y., and Merrill, A.H., Jr. (2011). Analysis of mammalian sphingolipids by liquid chromatography tandem mass spectrometry (LC-MS/MS) and tissue imaging mass spectrometry (TIMS). Biochim. Biophys. Acta *1811*, 838–853.
42. Waterhouse, A.M., Procter, J.B., Martin, D.M.A., Clamp, M., and Barton, G.J. (2009). Jalview Version 2--a multiple sequence alignment editor and analysis workbench. Bioinformatics *25*, 1189–1191.
43. Waggoner, D.W., Xu, J., Singh, I., Jasinska, R., Zhang, Q.X., and Brindley, D.N. (1999). Structural organization of mammalian lipid phosphate phosphatases: implications for signal transduction. Biochim. Biophys. Acta *1439*, 299–316.
44. Neuwald, A.F. (1997). An unexpected structural relationship between integral membrane phosphatases and soluble haloperoxidases. Protein Sci. *6*, 1764–1767.
45. Denny, P.W., Shams-Eldin, H., Price, H.P., Smith, D.F., and Schwarz, R.T. (2006). The protozoan inositol phosphorylceramide synthase: a novel drug target that defines a new class of sphingolipid synthase. J. Biol. Chem. *281*, 28200–28209.
46. Kol, M., Panatala, R., Nordmann, M., Swart, L., van Suijlekom, L., Cabukusta, B., Hilderink, A., Grabietz, T., Mina, J.G.M., Somerharju, P., et al. (2017). Switching head group selectivity in mammalian sphingolipid biosynthesis by active-site-engineering of sphingomyelin synthases. J. Lipid Res. *58*, 962–973.
47. Goren, M.A., Nozawa, A., Makino, S.i., Wrobel, R.L., and Fox, B.G. (2009). Cell-free translation of integral membrane proteins into unilamelar liposomes. Methods Enzymol. *463*, 647–673.
48. Gruenheit, N., Baldwin, A., Stewart, B., Jaques, S., Keller, T., Parkinson, K., Salvidge, W., Baines, R., Brimson, C., Wolf, J.B., et al. (2021). Mutant resources for functional genomics in Dictyostelium discoideum using REMI-seq technology. BMC Biol. *19*, 172.
49. Sato, K., Noda, Y., and Yoda, K. (2009). Kei1: a novel subunit of inositolphosphorylceramide synthase, essential for its enzyme activity and Golgi localization. Mol. Biol. Cell *20*, 4444–4457.
50. Takesako, K., Kuroda, H., Inoue, T., Haruna, F., Yoshikawa, Y., Kato, I., Uchida, K., Hiratani, T., and Yamaguchi, H. (1993). Biological properties of aureobasidin A, a cyclic depsipeptide antifungal antibiotic. J. Antibiot. *46*, 1414–1420.
51. Heidler, S.A., and Radding, J.A. (1995). The AUR1 gene in Saccharomyces cerevisiae encodes dominant resistance to the antifungal agent aureobasidin A (LY295337). Antimicrob. Agents Chemother. *39*, 2765–2769.
52. Barisch, C., Kalinina, V., Lefrançois, L.H., Appiah, J., López-Jiménez, A.T., and Soldati, T. (2018). Localization of all four ZnT zinc transporters in Dictyostelium and impact of ZntA and ZntB knockout on bacteria killing. J. Cell Sci. *131*, jcs222000.
53. Gräf, R., Daunderer, C., and Schliwa, M. (1999). Cell cycle-dependent localization of monoclonal antibodies raised against isolated Dictyostelium centrosomes. Biol. Cell *91*, 471–477.
54. Lima, W.C. (2019). The AK426 antibody recognizes the Golgi apparatus in Dictyostelium cells by immunofluorescence. Antib. Rep. *2*, e59.
55. Merlot, S., Meili, R., Pagliarini, D.J., Maehama, T., Dixon, J.E., and Firtel, R.A. (2003). A PTEN-related 5-phosphatidylinositol phosphatase localized in the Golgi. J. Biol. Chem. *278*, 39866–39873.
56. Neuhaus, E.M., Horstmann, H., Almers, W., Maniak, M., and Soldati, T. (1998). Ethane-freezing/methanol-fixation of cell

monolayers: a procedure for improved preservation of structure and antigenicity for light and electron microscopies. J. Struct. Biol. *121*, 326–342.
57. Ravanel, K., de Chassey, B., Cornillon, S., Benghezal, M., Zulianello, L., Gebbie, L., Letourneur, F., and Cosson, P. (2001). Membrane sorting in the endocytic and phagocytic pathway of Dictyostelium discoideum. Eur. J. Cell Biol. *80*, 754–764.
58. Ellingson, J.S. (1974). Changes in the phospholipid composition in the differentiating cellular slime mold, Dictyostelium discoideum. Biochim. Biophys. Acta *337*, 60–67.
59. Jiménez-Rojo, N., and Riezman, H. (2019). On the road to unraveling the molecular functions of ether lipids. FEBS Lett. *593*, 2378–2389.
60. Torgersen, M.L., Klokk, T.I., Kavaliauskiene, S., Klose, C., Simons, K., Skotland, T., and Sandvig, K. (2016). The anti-tumor drug 2-hydroxyoleic acid (Minerval) stimulates signaling and retrograde transport. Oncotarget *7*, 86871–86888.
61. Goldfine, H. (2010). The appearance, disappearance and reappearance of plasmalogens in evolution. Prog. Lipid Res. *49*, 493–498.
62. Raetz, C.R., and Dowhan, W. (1990). Biosynthesis and function of phospholipids in Escherichia coli. J. Biol. Chem. *265*, 1235–1238.
63. Goh, E.X.Y., and Guan, X.L. (2021). Targeted Lipidomics of Drosophila melanogaster During Development. Methods Mol. Biol. *2306*, 187–213.
64. Weeks, G., and Herring, F.G. (1980). The lipid composition and membrane fluidity of Dictyostelium discoideum plasma membranes at various stages during differentiation. J. Lipid Res. *21*, 681–686.
65. Marquês, J.T., Marinho, H.S., and de Almeida, R.F.M. (2018). Sphingolipid hydroxylation in mammals, yeast and plants - An integrated view. Prog. Lipid Res. *71*, 18–42.
66. Rennie, E.A., Ebert, B., Miles, G.P., Cahoon, R.E., Christiansen, K.M., Stonebloom, S., Khatab, H., Twell, D., Petzold, C.J., Adams, P.D., et al. (2014). Identification of a sphingolipid α-glucuronosyltransferase that is essential for pollen function in Arabidopsis. Plant Cell *26*, 3314–3325.
67. Wang, W., Yang, X., Tangchaiburana, S., Ndeh, R., Markham, J.E., Tsegaye, Y., Dunn, T.M., Wang, G.L., Bellizzi, M., Parsons, J.F., et al. (2008). An inositolphosphorylceramide synthase is involved in regulation of plant programmed cell death associated with defense in Arabidopsis. Plant Cell *20*, 3163–3179.
68. Berchtold, D., Piccolis, M., Chiaruttini, N., Riezman, I., Riezman, H., Roux, A., Walther, T.C., and Loewith, R. (2012). Plasma membrane stress induces relocalization of Slm proteins and activation of TORC2 to promote sphingolipid synthesis. Nat. Cell Biol. *14*, 542–547.
69. Hashida-Okado, T., Ogawa, A., Endo, M., Yasumoto, R., Takesako, K., and Kato, I. (1996). AUR1, a novel gene conferring aureobasidin resistance on Saccharomyces cerevisiae: a study of defective morphologies in Aur1p-depleted cells. Mol. Gen. Genet. *251*, 236–244.
70. Di Francesco, A., Zajc, J., and Stenberg, J.A. (2023). Aureobasidium spp.: Diversity, Versatility, and Agricultural Utility. Horticulturae *9*, 59.
71. Gabriel, D., Hacker, U., Köhler, J., Müller-Taubenberger, A., Schwartz, J.M., Westphal, M., and Gerisch, G. (1999). The contractile vacuole network of Dictyostelium as a distinct organelle: its dynamics visualized by a GFP marker protein. J. Cell Sci. *112*, 3995–4005.
72. Sutterwala, S.S., Hsu, F.F., Sevova, E.S., Schwartz, K.J., Zhang, K., Key, P., Turk, J., Beverley, S.M., and Bangs, J.D. (2008). Developmentally regulated sphingolipid synthesis in African trypanosomes. Mol. Microbiol. *70*, 281–296.
73. MacLean, B., Tomazela, D.M., Shulman, N., Chambers, M., Finney, G.L., Frewen, B., Kern, R., Tabb, D.L., Liebler, D.C., and MacCoss, M.J. (2010). Skyline: an open source document editor for creating and analyzing targeted proteomics experiments. Bioinformatics *26*, 966–968.
74. Peng, B., Kopczynski, D., Pratt, B.S., Ejsing, C.S., Burla, B., Hermansson, M., Benke, P.I., Tan, S.H., Chan, M.Y., Torta, F., et al. (2020). LipidCreator workbench to probe the lipidomic landscape. Nat. Commun. *11*, 2057.
75. Sigrist, C.J.A., de Castro, E., Cerutti, L., Cuche, B.A., Hulo, N., Bridge, A., Bougueleret, L., and Xenarios, I. (2013). New and continuing developments at PROSITE. Nucleic Acids Res. *41*, D344–D347.
76. Möller, S., Croning, M.D., and Apweiler, R. (2001). Evaluation of methods for the prediction of membrane spanning regions. Bioinformatics *17*, 646–653.
77. Jumper, J., Evans, R., Pritzel, A., Green, T., Figurnov, M., Ronneberger, O., Tunyasuvunakool, K., Bates, R., Žídek, A., Potapenko, A., et al. (2021). Highly accurate protein structure prediction with AlphaFold. Nature *596*, 583–589.
78. Katoh, K., Rozewicki, J., and Yamada, K.D. (2019). MAFFT online service: multiple sequence alignment, interactive sequence choice and visualization. Brief. Bioinform. *20*, 1160–1166.
79. Schindelin, J., Arganda-Carreras, I., Frise, E., Kaynig, V., Longair, M., Pietzsch, T., Preibisch, S., Rueden, C., Saalfeld, S., Schmid, B., et al. (2012). Fiji: an open-source platform for biological-image analysis. Nat. Methods *9*, 676–682.
80. Eising, S., Thiele, L., and Fröhlich, F. (2019). A systematic approach to identify recycling endocytic cargo depending on the GARP complex. Elife *8*, e42837.
81. Fröhlich, F., Petit, C., Kory, N., Christiano, R., Hannibal-Bach, H.K., Graham, M., Liu, X., Ejsing, C.S., Farese, R.V., and Walther, T.C. (2015). The GARP complex is required for cellular sphingolipid homeostasis. Elife *4*, e08712.
82. Han, X. (2016). Fragmentation Patterns of Sphingolipids. In Lipidomics: Comprehensive Mass Spectrometry of Lipids (Willey). https://doi.org/10.1002/9781119085263.
83. Bartlett, E.M., and Lewis, D.H. (1970). Spectrophotometric determination of phosphate esters in the presence and absence of orthophosphate. Anal. Biochem. *36*, 159–167.
84. Hagedorn, M., Neuhaus, E.M., and Soldati, T. (2006). Optimized fixation and immunofluorescence staining methods for Dictyostelium cells. Methods Mol. Biol. *346*, 327–338.
85. Krogh, A., Larsson, B., von Heijne, G., and Sonnhammer, E.L. (2001). Predicting transmembrane protein topology with a hidden Markov model: application to complete genomes. J. Mol. Biol. *305*, 567–580.

STAR★METHODS

KEY RESOURCES TABLE

REAGENT or RESOURCE	SOURCE	IDENTIFIER
Antibodies		
V5 Tag Monoclonal Antibody (SV5-Pk1)	Thermo Fisher Scientific	R960-25
Anti-vatA	Geneva antibody facility	AJ520-H1
Anti-vacA	Geneva antibody facility	RB256-M2a
Anti-vacB	Geneva antibody facility	RB259-M2a
Anti-p80	Geneva antibody facility	AJ154-H1
Anti-Golgi	Geneva antibody facility	AK426-M2a
Anti-PorA	Geneva antibody facility	AK421-IgG2a
Anti-PDI	Markus Maniak (University of Kassel, Germany)	221-64-1
CF488A Goat Anti-Mouse IgG (H + L), Highly Cross-Adsorbed	Biotium	BOT-20018; RRID: AB_10557263
CF640R Goat Anti-Human IgG (H + L), Highly Cross-Adsorbed	Biotium	BOT-20081-1; RRID: AB_10854076
CF640R Goat Anti-Guinea Pig IgG (H + L), Highly Cross-Adsorbed	Biotium	BOT-20494
Bacterial and virus strains		
E. coli DH5alpha	Stock of the Molecular Cell Biology Division, University of Osnabrück	N/A
Chemicals, peptides, and recombinant proteins		
SP6 RNA Polymerase (20 U/μL)	Thermo Fisher Scientific	EP0131
WEPRO2240 wheat germ extract (WGE)	CellFree Sciences, Ltd	16DQ02
Aureobasidin A (AbA)	Takara Bio	630466
Critical commercial assays		
Pierce™ BCA Protein Assay Kits	Thermo Fisher Scientific	A55865
Experimental models: Cell lines		
AX2, wt, parental strain	Günther Gerisch	N/A
CSS2-mCherry, G418r	This study	N/A
mCherry-CSS2, G418r	This study	N/A
CSS2-mCherry ZntD-GFP, G418r, Hygr	This study	N/A
mCherry-CSS2 ZntD-GFP, G418r, Hygr	This study	N/A
Oligonucleotides		
Primers for pDM1208 (fwd), see STAR Methods	This study	oMIB154
Primers for pDM1208 (rev), see STAR Methods	This study	oMIB155
Primers for pDM1210 (fwd), see STAR Methods	This study	oMIB156
Primers for pDM1210 (rev), see STAR Methods	This study	oMIB157
Recombinant DNA		
CSS2-mCherry, pDM1210	This study	
mCherry-CSS2, pDM1208	This study	
ZntD-GFP, pDM1045	This study	N/A
EU-Flexi-CSS1, Ampr	This study	N/A

(*Continued on next page*)

Continued

REAGENT or RESOURCE	SOURCE	IDENTIFIER
pEU-Flexi-CSS2, Ampr	This study	N/A
pEU-Flexi-SMS2, Ampr	Kol et al.[46]	
Software and algorithms		
Bioicons		https://bioicons.com/
Skyline	MacLean et al.[73]	https://skyline.ms/project/home/begin.view
LipidCreator	Peng et al.[74]	https://lifs-tools.org/lipidcreator.html
LipidSearch™ 5.0	Thermo Fisher Scientific	N/A
FreeStyle™ 1.8 SP2	Thermo Fisher Scientific	N/A
Prosite	Sigrist et al.[75]	https://prosite.expasy.org/
TMHMM 2.0	Möller et al.[76]	https://services.healthtech.dtu.dk/services/TMHMM-2.0/
AlphaFold	Jumper et al.[77]	https://alphafold.ebi.ac.uk/
MAFFT version 7	Katoh et al.[78]	https://mafft.cbrc.jp/
Fiji (ImageJ 1.53t)	Schindelin et al.[79]	https://fiji.sc/
Imaris v9.8.2	Bitplane Switzerland	http://www.bitplane.com/imaris/imaris
Huygens Remote Manager v3.10	Scientific Volume Imaging	http://svi.nl
Adobe Illustrator 28.5 (2024)	Adobe	https://www.adobe.com/de/products/illustrator/
Other		
HL5c (complex medium)	Formedium	HLH3
SIH (defined medium)	Formedium	SIH0101
LoFlo (imaging medium)	Formedium	LF0501
NBD-C6-Ceramide	Invitrogen™	N1154
LightSPLASH® LIPIDOMIX®	Avanti Polar Lipids	330732
C17 Ceramide (d18:1/17:0)	Avanti Polar Lipids	860517P
Egg PC	Avanti Polar Lipids	131601
Wheat germ PI	Lipid Products (discontinued)	#1408
DOPE	Avanti Polar Lipids	850725

RESOURCE AVAILABILITY

Lead contact

Further information and requests for resources and reagents should be directed to the lead contact, Caroline Barisch (caroline.barisch@cssb-hamburg.de).

Materials availability

All materials generated in this study are available from lead contact upon reasonable request.

Data and code availability

All data of the lipidomics analyses can be found in the supplementary data files. Any additional information required to reanalyse the data presented in this paper can be obtained from the lead contact upon request.

EXPERIMENTAL MODEL

D. discoideum strains and cell culture

All the *D. discoideum* material used in this study is listed in the key resources table. Wild type (AX2) was grown under static condition in a 10-cm dish at RT in 10 mL of HL5c medium (Formedium) supplemented with P/S (100 U/ml penicillin and 100 mg/mL streptomycin).

To create CSS2-overexpressing cells, *css2* (DDB_G0268928) was amplified from *D. discoideum* cDNA and cloned into N- and C-terminal mCherry-fusion plasmids pDM1208 and pDM1210, respectively. The primers for cloning into pDM1208 were oMIB154 (5′-AGATCTATGG

GAGTACAACAACAATCGG-3′) and oMIB155 (5′-ACTAGTCTATTTATTATTAAATT TTGATAAAATATTTTG-3′), while the primers for pDM1210 cloning were oMIB156 (5′-AGATCTAAAA TGGGAGTACAACAACAATCGG-3′) and oMIB157 (5′ ACTAGTTTTATTATTAAATTTTG ATAAAA TATTTTG-3′). To generate the ZntD-GFP construct, ZntD was cleaved with SpeI and BglII from pDM1044-ZntD-mCherry[52] and cloned into pDM1045.

All plasmids used in this study are listed in the key resources table. Plasmids were electroporated into *D. discoideum* and selected with the appropriate antibiotic. Hygromycin was used at a concentration of 50 μg/mL, and neomycin (G418) at a concentration of 5 μg/mL.

METHOD DETAILS

Lipidomics

The Lipidomics Minimal Reporting Checklist (Lipidomics Standards Initiative (LSI, https://lipidomicstandards.org) can be found in Data S1/Methods S1. To prepare cells for lipidomics, cells were passed in either defined SIH or complex HL5c medium (both from Formedium) for six days. Indicated cells were treated additionally with 25 μM of AbA for 24 and 48 h, respectively. Confluent plates were harvested, washed and re-suspended in ice-cold Sorensen buffer (SB). The cell suspensions were directly snap-frozen and stored at −80°C prior to extraction. For normalization, the protein concentration was determined using the Pierce BCA protein kit (Thermo Fisher Scientific).

For the LC/MS-MS lipidomics analysis, cell suspensions containing 200 μg of protein were mixed with 150 mM ammonium formate and subjected to lipid extraction using $CHCl_3$/MeOH (2:1, v/v) following the protocol from Folch et al.[40,80] Cer (18:1/17:0) was spiked to each sample as internal standard. Lipids were dried and subsequently dissolved with 50:50 mix of mobile phase A (60:40 water/acetonitrile, 10 mM ammonium formate, 0.1% formic acid) and mobile phase B (88:10:2 2-propanol/acetonitrile/H_2O, 2 mM ammonium formate, 0.02% formic acid) before the analysis. For quantification, serial dilutions of LightSPLASH LIPIDOMIX (Avanti Polar Lipids) were injected alongside the samples as external standards.

For the identification of IPCs and Cers, suspensions containing 60 μg of protein were subjected to lipid extraction and alkaline hydrolysis using dichloromethane/methanol (1:2, v/v) following a protocol described by Sullard et al.[41,81] Also here, Cer (18:1/17:0) was added as internal standard. Subsequently, samples were mixed with 150 mM ammonium formate and organic solvents and mixed overnight at 48°C. Afterward, 150 μL 1 M KOH were added and incubated for another 2 h at 37°C under shaking conditions to hydrolyze glycerophospholipids. After neutralization with glacial acetic acid, the mixture was centrifuged and the supernatant was transferred to a new glass vial, dried, and re-suspended with a 65:35 mixture of mobile phase A and B (see above).

The HPLC run was performed using a C30 reverse-phase column (Thermo Acclaim C30, 2.1 × 250 mm, 3 μm, operated at 40°C; Thermo Fisher Scientific) connected to a Shimadzu LC-20AD HPLC system. A binary solvent system was used (mobile phases A and B) in a 20 min gradient at a flow rate of 300 μL/min. The HPLC was connected to a QExactivePLUS orbitrap mass spectrometer (Thermo Fisher Scientific) equipped with a heated electrospray ionization (HESI) probe. The maximum injection time for full scans was 100 ms with a target value of 3,000,000 at a resolution of 70,000 at m/z 200 and a mass range of 200–1200 m/z in positive and negative ion mode. The 5 and 10 most intense ions from the survey scan were selected and fragmented with high-energy collision dissociation with normalized collision energy of 25, 30, 35 (samples extracted with Folch) and 25, 30 (samples extracted with Sullards), respectively. Target values for MS/MS were set at 100,000 with a maximum injection time of 50 ms at a resolution of 35,000 at *m/z* 200.

For the quantification of total lipids, PIs, and ether/ester lipids, peaks were analyzed using the Lipid Search algorithm (Thermo Fisher Scientific). Product ion (MS2) and precursor ion (MS1) peaks were defined from scanning through raw files. From the intensities of lipid standards, the absolute values for each lipid classes in mol % were calculated. SM, PC, LPC, DAG, TAG and Cer were acquired in the positive ion mode, while PE, PI, PG, PS and LPE were acquired in negative ion mode. Candidate molecular species were identified by a database search for positive ($^+H^+$; $^+NH4^+$) or negative ion adducts ($^-H^-$; $^+COO^-$). Mass tolerance was set to 20 ppm and 5 ppm for the precursor mass from the positive ion mode and the negative ion mode, respectively. For the peak alignment between samples, the retention time (RT) tolerance were set to 0.5 and 0.21 min for the positive and negative ion mode, respectively. Samples were aligned within a time window and results were combined in a single report.

For the quantification of IPC from samples extracted by Folch extraction, the software FreeStyle 1.8 SP2 (Thermo Fisher Scientific) was used. To this end, the peak area of precursor ions normalized to the internal standard were calculated. For the quantification of IPC and Cer from samples extracted by Sullards, the peaks were analyzed with Skyline.[73,74] The top thirteen most abundant IPC species were selected. To confirm that the quantified peak represents IPC, the presence of MS/MS fragments characteristic to IPC (m/z 241 representing the inositol-1,2-cyclic phosphate anion and m/z 259 representing the inositol monophosphate anion) in all IPC species was checked.[82] The peak area of precursor ions from each IPC species was normalized against the total IPC signal from each sample. The complete dataset of the lipidomics analysis is shown in Table S2.

Preparation of liposomes

Liposomes were prepared as previously described.[46] Briefly, phospholipid stocks were prepared in $CHCl_3$:MeOH (9:1, v/v) and stored at −20°C. The phospholipid concentration was determined following Bartlett and Lewis.[83] Using a mini extruder (Avanti Polar Lipids), unilamellar liposomes were produced from a defined lipid mixture as stated in the figure legends: egg PC: DOPE: wheat germ PI 2:2:1 mol %, egg PC: DOPE 1:1 mol %; egg PC: wheat germ PI 1:1 mol %; and DOPE: wheat germ PI 1:1 mol %. To create a thin lipid film, 20 μmol of total lipids were dried with nitrogen gas. Dried lipids were re-suspended in 1 mL lipid rehydration buffer (25 mM HEPES (pH 7.5) and 100 mM NaCl) to create a 20 mM lipid suspension. After six freeze-thaw cycles, liposomes were extruded through 0.4 μM and 0.1 μM polycarbonate

membrane filter (Whatman-Nucleopore) to obtain an average diameter of 100 nm. Liposome suspensions were snap-frozen and stored at −80°C.

CFE and CSS activity assay

The cell-free expression (CFE) of CSS was performed as previously described.[46] Briefly, proteinase K was used to remove trace amounts from RNAse from pEU-Flexi-CSS1, pEU-Flexi-CSS2 and pEU-Flexi-SMS2 expression constructs (key resources table). CSS1 and CSS2 were synthesised together with a V5-tag using GeneArt DNA Synthesis (Thermo Fisher Scientific) and then cloned into pEU-Flexi. After phenol/$CHCl_3$ extraction, the constructs were dissolved in water at 1.8 μg/μL. The mRNA was transcribed in a 120 μL reaction volume containing 21.6 μg of DNA; 2 mM each of ATP, GTP, CTP, and 321'UTP; 45.6 units of SP6 RNA polymerase; 96 units of RNase inhibitor in 80 mM HEPES-KOH (pH 7.8); 20 mM of Mg-acetate; 2 mM of spermidine hydrochloride and 10 mM of DTT.[47] After a 4 h incubation at 37°C and a centrifugation at 3,400 xg for 5 min at RT, the supernatant was harvested and subsequently used for the cell-free translation reaction. Each 100 μL translation reaction contained: 2 mM of liposomes, 40 μg/mL of creatine kinase, 15 OD_{260} of WEPRO2240 WGE, 0.3 mM each of all 20 amino acids, 5 mM of HEPES-KOH (pH 7.8), 50 mM of potassium acetate, 1.25 mM of Mg-acetate, 0.2 mM of spermidine, 0.6 mM of ATP, 125 μM of GTP, 8 mM of creatine phosphate and 20 μL of the mRNA-containing supernatant. The translation mixture was then incubated for 4 h at 26°C. The translation products were directly used for the CSS assay. Protein expression was confirmed using western blots and anti-V5.

For the CSS activity assay, the reaction volume was set to 100 μL: 50 μL of the CFE product were incubated first with 5 μM of NBD-Cer, 25 mM of HEPES (pH 7.4), 75 mM of NaCl and 1 mM of $MgCl_2$ for 10 min on ice. This was followed by a 60 min incubation at 22°C under shaking condition. When indicated, Aba was added, ethanol served as vehicle control. The reaction was terminated by adding 375 μL of $CHCl_3$:MeOH (1:2, v/v) and stored at −20°C prior to lipid extraction and TLC analysis.[46] Where indicated *D. discoideum* and yeast lysates were generated. The preparation of the post-nuclear supernatant fraction of *D. discoideum* and *S. cerevisiae* was performed as described previously.[46]

Live fluorescence microscopy

To monitor the subcellular distribution of CSS2-mCherry or mCherry-CSS2 by live imaging, cells were transferred to either 4- or 8-well μ-slides (ibidi) and imaged in low fluorescent medium (LoFlo, Foremedium) with a Zeiss Cell observer spinning disc (SD) microscope using the 63x oil objective (NA 1.46). Images were further processed and analyzed with ImageJ.

Bead phagocytosis and immunofluorescence

The anti-VatA, anti-VacA, anti-VacB, anti-p80, anti-Golgi and anti-porA antibodies were obtained from the Geneva antibody facility (Geneva, Switzerland). The anti-PDI antibody was provided by Markus Maniak (University of Kassel, Germany). As secondary antibodies, anti-mouse and anti-human IgG or anti-guinea pig IgG coupled to CF488R (Biotium) or CF640R (Biotium) were used.

To prepare cells for IF, *D. discoideum* was fixed with with cold MeOH or PFA/picric acid as described previously.[84] Where indicated, cells were incubated overnight with 3 μm latex beads (Sigma Aldrich) before the fixation. Cells were embedded using ProlongGold antifade with DAPI (Molecular Probes). Images were recorded with a Zeiss Airyscan LSM880 confocal microscope and the 63x Plan-Apochromat 1.4 NA oil immersion objective or with an Olympus LSM FV-3000 confocal microscope and the 60×1.4 NA oil immersion objective. To improve signal-to-noise, indicated images were deconvolved using Huygens Remote Manager v3.10 from Scientific Volume Imaging (Netherlands). The images were further processed and analyzed with ImageJ/Fiji,[79] Inkscape and Adobe Illustrator. 3D-models were generated using Imaris version 9.8.2 from Bitplane (Switzerland).

SDS-PAGE and western blotting

For western blotting of mCherry-tagged CSS2, cells were washed, harvested and incubated with 2x Laemmli buffer. For western blotting of V5-tagged proteins, samples were added to urea buffer containing 5% β-mercaptoethanol instead. After SDS-PAGE, proteins were transferred for 50 min at 120 V to a nitrocellulose membrane (Amersham Protran, Premium 0.45 μm NC). To check the efficiency, Ponceau S staining was performed. For the detection of mCherry-tagged proteins, the membranes were blocked and incubated with an anti-mCherry primary (Rockland) and a goat anti-rabbit secondary antibody coupled to horseradish peroxidase (HRP) (BioRad). For V5-tagged proteins, an anti-V5 primary (Invitrogen; 1:4000) and a goat anti-mouse secondary antibody coupled to horseradish peroxidase (HRP) (BioRad, 1:4000) were used. The detection of HRP was accomplished using the Pierce ECL Western Blotting Substrate (Thermo Scientific).

Selection and prediction of D. discoideum CSS

The *D. discoideum* AX4 proteome was downloaded from UniProt (ID: UP000002195) and searched using Prosite (https://prosite.expasy.org/)[75] for the presence of the H-X3-D-X3-[GA]-X3-[GSTA] motif. The FASTA files of all 52 protein hits were compiled and submitted as queries to TMHMM 2.0[76] to search for the presence of TMDs.[85] Proteins with >3 TMDs were selected for further screening. Among the seven remaining candidates, proteins with known biochemical function (with annotation at dictybase.org or identification by BLAST search) were excluded yielding two potential CSS candidates.

AlphaFold was used to predict the membrane topology of *Dd*CSS1 and *Dd*CSS2.[77] MAFFT version 7 algorithm (https://mafft.cbrc.jp/) was used to construct phylogenetic tree and protein sequences.[78] The following parameters was adopted for MAFFT alignment: G-INS-i strategy, unalignlevel 0.0 and "try to align gappy regions away". NJ conserved sites and the JTT substitution model was used to generate a phylogenetic tree in phylo.ilo. Numbers on the branches indicate bootstrap support for nodes from 100 bootstrap replicates.

QUANTIFICATION AND STATISTICAL ANALYSIS

For the lipidomics analysis, each sample was spiked with Cer (18:1/17:0) as an internal standard. To enable accurate quantification, serial dilutions of LightSPLASH LIPIDOMIX (Avanti Polar Lipids) were used as external standards. Detailed steps of the quantification process are provided in the "lipidomics" section of the Methods. The experiment of Figure S6B was quantified by comparing the peak areas of IPC (38:0; 4) and IPC (40:0; 4) in cells treated with AbA or without. Statistics were assessed with a paired t-test. ns: non-significant.

All microscopy images were analyzed and processed using ImageJ/Fiji. The experiment of Figure S8C was quantified manually. The statistical differences was calculated with an unpaired t-test (****: *p*-value <0.0001). "n" indicates the number of independent biological replicates. SD: standard deviation.